

Mercury's Weather-beaten Surface: Understanding Mercury in the Context of Lunar and Asteroid Space Weathering Studies

Deborah L. Domingue

Planetary Science Institute, 1700 E. Fort Lowell, Suite 106, Tucson, AZ 85719-2395 USA
410-868-2296

domingue@psi.edu

Clark R. Chapman

Suite 300 Southwest Research Institute, 1050 Walnut Street, Boulder, CO 80302, USA

Rosemary M. Killen

NASA Goddard Space Flight Center, Greenbelt, MD 20771 USA

Thomas H. Zurbuchen

Department of Atmospheric, Oceanic, and Space Sciences, University of Michigan, Ann Arbor, MI 48109, USA

Jason A. Gilbert

Department of Atmospheric, Oceanic, and Space Sciences, University of Michigan, Ann Arbor, MI 48109, USA

Menelaos Sarantos

Heliophysics Science Division, NASA Goddard Space Flight Center, Greenbelt, MD 20771, USA

Mehdi Benna

NASA Goddard Space Flight Center, Greenbelt, MD 20771 USA

James A. Slavin

Heliophysics Science Division, NASA Goddard Space Flight Center, Greenbelt, MD 20771, USA

Thomas M. Orlando

School of Chemistry and Biochemistry and School of Physics, Georgia Institute of Technology, Atlanta, GA 30332-0400, USA

David Schriver

Institute of Geophysics and Planetary Physics, University of California, 3871 Slichter Hall, Los Angeles, CA 90024, USA

Ann L. Sprague

University of Arizona, Lunar and Planetary Laboratory, 1629 E. University Blvd., Tucson, AZ 85721-0092, USA

David T. Blewett

Johns Hopkins University Applied Physics Laboratory, Laurel, MD 20723, USA

Jeffrey J. Gillis-Davis

Hawai'i Institute of Geophysics and Planetology, University of Hawai'i, 1680 East-West Road, Post 515, Honolulu, HI 96822, USA

William C. Feldman

Planetary Science Institute, 1700 E. Fort Lowell, Suite 106, Tucson, AZ 85719-2395 USA

David J. Lawrence

Johns Hopkins University Applied Physics Laboratory, Laurel, MD 20723, USA

George C. Ho

Johns Hopkins University Applied Physics Laboratory, Laurel, MD 20723, USA

Faith Vilas

Planetary Science Institute, 1700 E. Fort Lowell, Suite 106, Tucson, AZ 85719-2395 USA

Carle M. Pieters

Department of Geological Sciences, Brown University, 324 Brook St., Box 1846, Providence, RI 02912, USA

William E. McClintock

Laboratory for Atmospheric and Space Physics, University of Colorado, Boulder, CO 80303, USA

Jorn Helbert

Institute for Planetary Research, DLR, Rutherfordstrasse 2, 12489 Berlin, Germany

ABSTRACT. Understanding the composition of Mercury's crust is key to comprehending the formation of the planet. The regolith, derived from the crustal bedrock, has been altered via a set of space weathering processes. These processes are the same set of mechanisms that work to form Mercury's exosphere, and are moderated by the local space environment and the presence of an intrinsic planetary magnetic field. The alterations need to be understood in order to determine the initial crustal compositions. The complex interrelationships between Mercury's exospheric processes, the space environment, and surface composition are examined and reviewed. The processes are examined in the context of our understanding of these same processes on the lunar and asteroid regoliths.

Keywords:

Mercury (planet)

Space weathering

Surface processes

Exosphere

Surface composition

Space environment

Introduction

Space weathering is a term used for a set of processes that affects the observable physical, chemical, and mineral properties of the surfaces of atmosphereless bodies. Much of what we know about surface compositions is garnered from remotely sensed reflectance spectra. Space weathering alters spectral signatures by: (1) darkening (lowering of the spectral albedo), (2) reducing spectral contrast (diminishing the strength of absorption features), and (3) reddening (increasing the slope of the continuum reflectance with increasing wavelength) (Adams and McCord 1973; Fischer and Pieters 1994). These effects must be factored into the interpretation of spectral measurements in terms of specific compositions.

The alterations by space weathering processes are tied to the exposure of a planetary surface to its space environment. Interplay between the space environment and surface also generates and maintains a surface-bounded exosphere, in the case of the Moon and Mercury. There are complex linkages between the space environment, weathering processes, exosphere, and evolution of the immediate surficial regolith (soil or particulate layer).

By “space environment” we mean exogenic processes including solar wind, solar and cosmic radiation, and interplanetary meteoritic and cometary debris impacting or bombarding the surface. The flux, energy, and composition of impacting particles each play a role in the type and magnitude of physical and chemical alteration of the surface, including sputtering, implantation, and volatilization. Also, a planet’s magnetic field can shield the surface or focus ions onto specific regions, thus influencing the magnitude of space weathering effects and possible regional variations.

Processes within Mercury’s system that link the exosphere, surface, and magnetopause of Mercury are summarized in Fig. 1 (Domingue et al., 2007). Similar processes modify the lunar regolith and generate the lunar exosphere. This system has usually been examined from a “look up” perspective; meaning examining the composition and physical, spatial, and temporal properties of exospheric constituents, what is removed from the surface. This paper examines the system from a “look down” perspective to understand the material that is left behind on the surface in creating the exosphere, and how it is altered, perhaps to maturity, by the same processes that generate the exosphere. While each process depicted in Fig. 1 affects the surface, the dominant alteration processes are believed to be micrometeoroid and solar wind ion bombardment (e.g. Hapke 2001). Due to Mercury’s proximity to the Sun, such processes as photon-stimulated desorption (PSD), electron-stimulated desorption (ESD), and

thermal desorption and cycling are also examined in detail. Of course, none of these processes works in isolation; their combined effects mature the surface and produce the observed exosphere.

Our understanding of the physical, chemical, and mineralogical effects of space weathering has largely come from examining lunar samples in conjunction with remote sensing observations of the Moon. Further insight is based on asteroid observations compared with meteorite measurements, from laboratory simulations of some space weathering processes, and from theoretical considerations. For instance, asteroids span a wide range of heliocentric distance extending to inside the orbit of Mercury, subjecting their surfaces to a wide range of fluxes and energies of micrometeoroids and solar wind particles. And they have long been known from spectral studies to be subject to space weathering processes (e.g. Chapman 2004), perhaps assisting extrapolating with semi-major axis some of our lunar understanding in to Mercury. Recently, much has been learned about how optical space weathering varies with size, location, composition, and age of diverse asteroids (Vernazza et al., 2009; Nesvorny et al. 2010). Asteroids range widely in size from bodies, like Vesta, that are sufficiently large that regolith processes are somewhat similar to those on the Moon (Housen et al. 1979), to sub-kilometer objects so small that they may lack regoliths of any type and are subject to non-intuitive processes in a microgravity environment (Scheeres et al. 2010). Asteroidal regoliths, like the lunar regolith, are also studied, from laboratory samples, to the degree that gas-rich regolith-breccia meteorites preserve relevant aspects of asteroid regoliths (they do *not* preserve the porous, particulate character of a surficial regolith). In addition, extremely high-resolution images of the surfaces of two asteroids, Eros and Itokawa, help to calibrate inferences and theories developed from more distant observations. Laboratory simulations of several space weathering processes using meteorites and other materials have expanded understanding of the effects of each process, the alteration rates, and their dependence on surface properties.

We examine Mercury's complex surface-exosphere-magnetosphere system in context of what we understand about space weathering based on the lunar and asteroid examples. Each process is discussed in terms of the relevant physics and the results of laboratory experiments. Mercury's unique space environment is considered, especially in light of observations during the recent MESSENGER flybys. The role of each process, in altering and maturing the surface, is considered within the context of Mercury's environment. Mercury's surface composition is compared and contrasted with lunar compositions and examined in light of space weathering effects.

The Processes

The processes in Fig. 1 fall into two main groups, those associated with micrometeoroid bombardment and those with solar radiation (particles and photons). While these processes are examined in isolation it is important to remember how each affects the other in understanding both exosphere formation and surface modification.

Based on laboratory measurements of lunar soil samples, most optical changes seen in space-weathered spectra can be attributed to the presence of sub-micron, nanometer-scale particles of metallic iron (Papike et al. 1981, Pieters et al. 2000, Taylor et al. 2000). Such “nano-phase” iron particles (npFe^0) are a by-product of many of the processes listed above. We discuss how npFe^0 is formed, process by process, in this section, based on lunar, asteroid, and laboratory studies with extrapolations and predictions for Mercury., (We save discussing properties of npFe^0 until a later section of Mercury’s surface properties and composition.).

Micrometeoroid bombardment

Regolith formation is the product of the comminution (reduction to smaller size, pulverizing to smaller bits) of the local bedrock and boulders by repeated impacts. While larger impacts dominate the excavation, fracturing, and comminution of bedrock, micrometeoroid impacts process the surface on the scale of soil grains. There are four key effects associated with micrometeoroid bombardment that play a significant role in the cycle of exosphere formation and surface maturation:

- § Gardening
- § Melt and vapor production
- § Chemical reduction (change in oxidation state) and devolatilization
- § Preferential processing by size and composition

The magnitude of each effect is governed by the micrometeoroid impactor flux and velocity, and by the target temperature and composition. These effects do not operate in isolation, so their mutual and combined effects must be considered. We consider each effect based on lunar studies, then discuss differences, extrapolations, and predictions for Mercury’s surface.

Gardening

Gardening is the continual process of burial and excavation by impacts of all sizes. which covers (to various depths) altered or weathered material and brings unaltered (or less

altered) material to the surface. Gardening tends to homogenize the regolith's top layers. Cintala (1992), in comparing and contrasting the micrometeoroid bombardment environments of the Moon and Mercury, calculated that the volume of material excavated by dust particles of the same mass is 7% higher on Mercury than the Moon. The higher impact velocity on Mercury is offset by its higher gravity, causing excavation of material to be nearly equivalent though melt and vapor production is much greater (Cintala 1992; see following section), thus, for constant flux, gardening of the lunar and Mercury regoliths is roughly identical (Cintala 1992). A more recent study (Marchi et al. 2005) of asteroidal impactors >1 cm in size, which can strike Mercury at higher velocities ($>20\%$ strike at >50 km/s and at even higher speeds near perihelion) indicates enhanced melt and vapor production. These impactors also cause appreciable loss of ejecta from Mercury into interplanetary space, only some of which later reaccretes (Gladman & Coffey 2009). Whatever the loss rate, the much greater impactor flux on Mercury compared with the Moon (see next section) results in a deeper regolith on Mercury due to the larger (> 1 cm) impactors.

For micrometeoroids < 1 cm, the balance between impact velocity and gravity implies equivalent excavation and retention of impactor material between the Moon and Mercury per impact. Lunar samples contain 1- 4 % meteoritic material (Haskin and Warren 1991). The order of magnitude (or more) greater impact flux on Mercury (see next section) translates into an order of magnitude greater overturn rate and retention of impactor material. Mercury's surface is postulated to contain 5 – 20% meteoritic materials (Noble et al. 2007).

Several source processes have been proposed to contribute to creating the sodium exospheres on the Moon and Mercury, including impact vaporization, ion-sputtering, PSD, ESD, and thermal vaporization. The efficiency of each process is affected and limited by the diffusion of species from the interiors to the surfaces of regolith grains and by the regolith gardening rate. Killen et al. (2007) argue that the gardening rate on Mercury would be equivalent to the overturn of a 1 cm thick layer of the regolith in 1.5×10^5 years with a 50% probability (compared with 10^6 years with 50% probability for the Moon, Heiken et al. 1991). Killen et al. (2004a) argue regolith gardening on Mercury is sufficiently efficient to bring to the surface fresh grains which have not been completely depleted in Na (while burying depleted grains) in order to produce the currently observed exospheric Na. In our “look down” approach, this implies that Mercury is being depleted in exospheric species (e.g. sodium, calcium, and magnesium) from both the immediate surface and some presently not well understood depth in its regolith.

Melt and Vapor Production

The production of impact melt and vapor depends on the composition of impactor and target, the flux of impactors, and the impactor velocity distribution. To first order, and for this discussion, we assume that impactor and surface composition is the same for the Moon and Mercury (later sections explore compositional differences).

Cintala (1992) compared the flux and velocity distributions of dust impactors for the Moon and Mercury, based on extrapolations of the observed meteor flux at the Earth (Zook 1975) and considering the varying spatial density of dust with distance from the Sun (Leinert et al. 1981). He found the flux at Mercury to be nearly 5.5 times greater than at the Moon and the mean impact velocity 60% greater. Borin et al. (2009) used measurements of the mass accretion rate of cosmic dust at 1 A.U. from the Long Duration Exposure Facility (LDEF) satellite (Love and Brownlee 1993) and found a mean impact velocity at Mercury ~30% higher than at the Moon with a mass flux 170 times that of Cintala (1992).

Mouawad et al. (2011) modeled both ground-based dayside observations acquired concurrently with MESSENGER MASCS nightside tail observation of exospheric sodium and placed an upper limit on the contribution from impact vaporization ($2.1 \times 10^6 \text{ cm}^{-2}\text{s}^{-1}$). Burger et al. (2010) used Monte Carlo models to describe the distribution of neutral sodium measured by MASCS during the first two flybys and derived an upper limit of 15% contribution to the sodium exosphere by impact vaporization for the regions observed. Bounding the contribution of impact vaporization to exosphere generation also bounds the contribution of this process to the modification of the surface. If impact vaporization were the only source mechanism for sodium on the nightside/tail region, then a rate on Mercury ~6 times a lunar value would account for the sodium measured by MASCS. Although this is commensurate with impact vaporization rates of ~0.6 to ~5 times the lunar value predicted by Morgan et al. (1988) and the flux and velocity predictions of Cintala (1992), it does not match the observed distribution on Mercury's dayside. An additional process, such as PSD, is required (Mouawad et al. 2011). In contrast, Borin et al.'s (2009) impact vaporization rate of ~170 times the lunar value does not reproduce either the amount or the distribution of sodium seen on either the day or night side (Mouawad et al. 2011). Mouawad et al. (2011) estimate an upper limit on the contribution of impact vaporization to the generation of the exosphere, thus its contribution to surface modification, more aligned with Cintala (1992) than Borin et al. (2009) but Borin et al. (2010) believe that "impact vaporization has a much higher contribution than previously assumed".

Cintala (1992) showed that varying impact velocity by a factor of 2 results in factors of ~3 in melt production and 4 to 5 in vapor production, thus ~15 or ~20 times more, respectively, per unit time, at Mercury compared with the Moon. The melt produces glasses within the regolith and the vapor produces coatings or patinas on nearby regolith grains along with additional glasses.

Two types of glasses in lunar soils are defined by differences in their shape and surface texture. The first are fairly regular spheres or ellipsoids with relatively smooth surfaces and mostly clast (rock or mineral fragment)-free, homogenous interiors (e.g. Apollo Soil Survey 1971, Delano 1986, Horz and Cintala 1997). These glasses can be either volcanic or produced by micrometeoroid impacts into crystalline rock surfaces (Horz and Cintala 1997).

The second type of glass is irregular in shape, often jagged, clast-laden, and frequently very vesicular (Horz and Cintala 1997). It is found in agglutinates (McKay et al. 1972), which are glassy, fused local soils constituting a major component of lunar regoliths (McKay et al., 1991; Horz and Cintala, 1997). Agglutinates form by the following impact process (McKay et al. 1991):

- § A high-velocity micrometeoroid impacts soil containing previously implanted solar wind elements, chiefly hydrogen and helium.
- § Grains are thereby melted, forming glass, and implanted solar wind elements are released.
- § The released hydrogen reacts with FeO in the glass, reducing it to metallic iron and producing water, which escapes from the glass.
- § Vesicles are formed in the glass by the released solar wind gases and possibly by the generated water vapor.
- § Iron droplets (npFe^0) formed by the reduction process are incorporated into the agglutinate.
- § The glass melt engulfs local, small soil grains before it cools.
- § The hot glass melt releases solar wind gases from the engulfed soil grains, possibly trapping some of these gases in the glass as it cools.

Up to half of sieve fractions <0.5 mm in size of many lunar soils are agglutinates (Heiken 1974, Morris et al. 1983, Horz and Cintala 1997). Fig. 2 shows examples of lunar agglutinates, revealing their shapes and textures. A ropy glass particle from an Apollo 12 soil sample is exemplified in Fig. 3; it is considered an impact product (McKay et al. 1991). The scanning electron micrograph shows the complex surface texture resulting from the welded coating of fine fragments. Cintala (1992) claims that a given impactor excavates about the same amount of material on the Moon and Mercury, but that the amount of melt produced on Mercury is twice the lunar value. The higher melt production may enhance the concentration of glass within Mercury's regolith compared with lunar soils, so Cintala (1992) argues that little crystalline material survives in the upper layers of Mercury's regolith. Mercury's glassy regolith should be highly reworked by melting and vaporization, solar wind implantation, and the combination of these processes, thus reducing the Fe^{2+} content of the glasses (Cintala 1992).

Impact-produced vapor also condenses on nearby regolith grains to produce coatings or patinas on the grains. In lunar soils these patinas are often reduced compared to grain interiors and contain npFe^0 . The size or depth of the vapor coating or rim is a function of the lifetime of the grain at the surface and the amount of vapor produced during the surface exposure time of the grain. While Cintala (1992) argues that the rim depth will be very small in both the lunar and Mercury cases, the amount of vapor produced on Mercury is an order of magnitude greater, implying a larger source for coating adjacent grains. This could potentially produce thicker rims on Mercury grains compared to the Moon, however it is difficult to factor in the number of impact events to which a grain is exposed to during its surface-residence lifetime. Examples of rims on lunar soil grains are shown in Fig. 4.

While a given impact mass may excavate nearly the same volume of regolith on Mercury and the Moon, the greater impact flux on Mercury will create a deeper regolith that is potentially more mixed simply due to the increased number of impacts.

Material Reduction and Devolatilization

Nano-phase metallic iron particles (npFe^0) form by reduction of FeO in lunar soils. Their presence causes most optical changes seen in space-weathered spectra (Papike et al. 1981, Pieters et al. 2000, Taylor et al. 2000). They occur in thin amorphous rims surrounding individual grains (Keller and McKay, 1993), and as inclusions in agglutinates. They exhibit two consistent properties: 1) they are usually relatively pure Fe, lacking the significant Ni and Co present in meteoritic metal, and 2) most are extremely fine-grained. Ferromagnetic

analysis shows that most metal is in the single-domain size range (3–10 nm) and thus is not always visible using an optical microscope (Morris, 1976; Keller and McKay, 1993). There is a bimodal distribution in npFe^0 size depending on its location. Those found in thin amorphous mineral coatings are ~ 3 nm diameter (Keller and Clemett, 2001) while those in agglutinates are twice as large (~ 7 nm) (Keller and Clemett, 2001). A transmission electron microscope (TEM) image of a lunar agglutinate in Fig. 5 shows the layer of fine-grained npFe^0 in the rim of the grain along with the coarser-grained npFe^0 within the agglutinate's interior.

Nanometer-scale metallic iron is mainly produced by (1) micrometeoroid bombardment and (2) solar wind ion implantation and sputtering (solar wind ion irradiation), which do not necessarily operate independently. We first discuss production in agglutinates and then in grain rims. Three models involving micrometeoroid bombardment have been advanced to explain the properties of npFe^0 in agglutinates, each requiring melting of the soil grains to form glass. The first model invokes the liberation of previously implanted solar wind H and He during target melting. The liberated H reacts with FeO in the glass, partly reducing it to metallic iron particles and producing some H_2O , which escapes from the glass (Housley et al., 1973a; Housley et al., 1973b).

The second model vaporizes volatile elements in the regolith by the intense, transient shock-wave of an impact; repeated impacts progressively deplete the maturing soil in more volatile elements so that a mature regolith is already reduced so that melting that forms agglutinates will simultaneously create npFe^0 (Hapke 2001). Measurements show (Epstein and Taylor, 1972) that the vaporization of the light isotopes, ^{16}O and ^{28}Si (or, conversely, a preferential condensation of the heavy isotopes, ^{18}O and ^{30}Si) is accompanied by a reduction of the bulk O/Si ratio (Hapke, 2001).

The third model is a two-stage process. First, micrometeoroid bombardment melts the finest fraction of the regolith (Papike et al. 1981, Pieters et al. 2000, Taylor et al. 2000), which has the highest concentration of npFe^0 within particle rims. Agglutinates are thus enriched in npFe^0 by the melting and incorporation of grains that already include npFe^0 ; concentration “coarsens” or makes larger the npFe^0 grains within agglutinates (Pieters et al. 2000, Noble and Pieters 2003). Although there is debate about which mechanism dominates in reducing Fe^{2+} to npFe^0 , all three models agree that production of nanophase Fe within agglutinates depends on (1) availability of Fe compounds in target soils and (2) melting by micrometeoroid impacts.

Turning to formation of npFe^0 within grain rims, there are also three models. The first two include impact-produced vapor deposition. This vapor condenses on nearby particles and

creates a patina or rim on regolith grains, but a reducing environment due to previously implanted solar H on the grain being coated forms npFe^0 . Alternatively, the vapor is produced at a sufficiently high temperature so that hydrogen implantation is not required to reduce the FeO present into metallic iron (Sasaki et al. 2001, Sasaki and Kurahasi 2004). Formation of vapor-deposit rims is a surface effect. Since the surface to volume ratio is greatest within the finer soil fractions, it is understandable that increased npFe^0 concentrations are found within the finer fractions of lunar soil samples.

The final concept for producing npFe^0 within grain rims, which does not require micrometeoroid impact and vapor production (and is invoked to explain space weathering on asteroids), is the irradiation of the top layers of regolith grains by solar wind ions. According to this idea, the bombardment of regolith grains by solar wind hydrogen produces a reducing environment. If FeO is present, then hydrogen implantation will reduce the FeO to Fe^0 , forming the single-domain, nanometer-scale metallic iron particles within the upper layers of the regolith grains (Hapke 2001).

Preferential Processing by Size and Composition

Not all minerals behave the same under comminution, melting, and vaporization processes. There is evidence in the lunar soils of mechanical fractionation by impacts. Lunar soils show enriched feldspar in the smaller size fractions relative to other minerals (Devine et al. 1982, Papike et al. 1982, McKay et al. 1991), attributed to the excellent cleavage inherent in feldspars (plagioclase) compared with other minerals (Basu 1976, Basu et al. 1975, Hörz et al. 1984). Also minerals that occur as very small grains in the parent rock are also concentrated in the finer fractions after comminution (e.g. Laul et al., 1981). Such effects are important since the fine fractions ($< 45\mu\text{m}$) dominate the spectral reflectance properties of lunar soils (Pieters, 1983, 1993, Pieters et al. 1993, Hapke 2001).

Melt fractionation also occurs (Lunar Soil Characterization Consortium: LSCC, Taylor et al. 2001a, 2001b, 2010), which is important in forming glasses, especially agglutinates. Models of lunar soil evolution incorporate melt fractionation to explain the following LSCC soil observations:

- § The agglutinitic glass component in soil separates increases with decreasing size fraction
- § The agglutinitic glass compositions form an apparent mixing line between the bulk highland and mare soil compositions

- § Agglutinitic glasses in mare soils are depleted in TiO_2
- § Agglutinitic glasses in highland soils are rich in basaltic components (FeO , TiO_2 , MgO)

Pieters and Taylor (2003) suggest these observations can be explained by a combination of mare-highland mixing and a proposed differential melting sequence of glass > plagioclase > pyroxene > ilmenite.

Lunar soils also exhibit vapor fractionation. Impact shock-wave heating vaporizes the more volatile elements in the regolith. Some vaporized elements escape lunar gravity so the soil becomes progressively more depleted in volatiles with increasing maturity (McKay et al. 1991). Non-escaping volatiles show a measureable mass fractionation of their isotopes. Epstein and Taylor (1972) showed that lunar soils are enriched in the heavier oxygen (^{18}O) and silica (^{30}Si) isotopes relative to crystalline rocks, and these enrichments are directly related to the amount of hydrogen in the soils (McKay et al. 1991). They also showed that enrichment of ^{18}O and ^{30}Si is a surface effect, and that oxygen preferentially escapes relative to silica in the fractional vaporization process (McKay et al. 1991), contributing to a reduced environment and production of npFe^0 . There is also an increased concentration of volatile elements (such as Zn, Ga, Ge, Cd, Sb, Te, and Hg) with decreasing soil size fraction (McKay et al. 1991). Such elements deposited on grain surfaces are thus enriched in the finer fractions due to their larger surface-to-volume ratio (Krähenbühl et al. 1977, McKay et al. 1991).

Solar radiation

In addition to micrometeoroids solar wind particles strike and help mature Mercury's and the Moon's surfaces and are perhaps the chief process altering asteroid surfaces. Main belt asteroid regoliths are less shocked than lunar counterparts (due to lower impact velocities) and less impact melts (and related products like agglutinates) are produced (Horz and Cintala 1997), as revealed by studies of gas-rich meteorite breccias, in which shock effects are mostly correlated with mechanical comminution and solid-state deformation (e.g. Stoffler et al. 1988, 1991; Keil et al. 1994). The rarity of agglutinitic particles in regolith breccia meteorites (Basu and McKay 1983; McKay et al. 1991; Noble et al. 2011) may also be due to effects of differential melting and inherent asteroid surface compositions. The scarce presence of npFe^0 particles in regolith breccia meteorites (Noble et al. 2010) indicates a different formation mechanism compared to the Moon. Regardless, asteroid reflectance spectra exhibit space weathering attributes, which for example, cause the spectral differences between ordinary

chondrite meteorites and many S-type asteroids, their presumed parent bodies. Solar wind ion irradiation has been argued to be the dominant mechanism weathering asteroid surfaces (Pieters et al. 2000, Chapman 2004; Vernazza et al. 2009).

In the post-Apollo program era, most asteroid regolith studies attempted to scale the developing understanding of lunar surface processes to bodies with lesser gravity (Housen et al. 1979, Langevin 1982, Housen 1982), different exposure to the solar wind (e.g. Anders 1975), and a different impact environment. Most applications were to relatively large, main-belt asteroids. Concurrently, discrepancies between asteroid and meteorite spectra led to speculations (Chapman & Salisbury 1973) that impact vitrification -- then the chief hypothesis for the reddening and darkening of lunar soils -- might explain the differences between spectra of common ordinary chondrites and the somewhat redder and darker S-type asteroids, the most common type of asteroid in the inner main belt. Binzel et al. (1996) showed that spectra of moderate-albedo near-Earth asteroids spanned a range between ordinary chondrite-like spectra and S-type spectra, implying that they were responding in an age-dependent way to a space-weathering process that caused their colors to evolve. Chapman (1996) showed that Galileo spectra of fresh ejecta from recent craters on Ida, as well as of Ida's satellite Dactyl, more closely resembled ordinary chondrite spectra than the more widespread, older S-type units on Ida implying an ongoing space-weathering process.

Successive laboratory studies (cf. Clark et al. 2002) show that simulated space-weathering processes indeed modify mineral spectra in the directions observed for asteroids. They indicate that solar wind irradiation operates on time scales of $10^4 - 10^6$ years, whereas micrometeoroid bombardment operates on longer time scales of $10^8 - 10^9$ years (Sasaki et al. 2001, Vernazza et al. 2009). Based on new dynamical analyses that can determine the ages of family-forming collisional break-ups (cf. Nesvorný et al. 2006), Vernazza et al. (2009) and others have measured spectra of very young asteroids showing that most spectral changes take place in an unexpectedly short time scale (< 1 Myr). Comparisons of spectral slope (between 500 and 900 nm) with family member age suggest that ion irradiation is rapid and dominates early in an asteroid's surface history, while slope changes due to micrometeoroids are gradual and dominate later (Strazulla et al. 2005, Vernazza et al. 2009). Willman et al. (2008) find that over long time scales (~ 500 Myr) asteroids gradually evolve from relatively mature colors to slightly more mature colors.

In order to better gauge the relative roles and alteration rates of solar wind particle and micrometeoroid bombardment on Mercury, we must understand the physical, chemical, and mineralogical changes induced by each process. We previously discussed micrometeoroids

and now turn our attention to particle irradiation. While many observational and laboratory studies of solar wind irradiation pertain to generating exospheres, we now examine corresponding surface effects in our “look down” approach from the following radiation processes:

- § Ion implantation
- § Physical sputtering
- § Chemical sputtering
- § Desorption induced by electronic transitions (DIET)
- § Thermal desorption

Ion implantation

Collisions between solar wind or magnetospheric ions in Mercury’s environment with the planet’s surface result in either implantation or sputtering. This section examines surface alteration and maturation by ion implantation while following sections examine sputtering by both physical and chemical mechanisms. Ion implantation refers to a collision between an impacting ion and a target regolith grain that results in the accommodation of the impacting ion within the grain’s atomic lattice. Behrisch and Wittmaack (1991) demonstrated that keV solar wind protons implant themselves to depths of a few hundred Angstroms into lunar soil regolith grains, thus implantation is mainly a surface effect. As such ions travel through grains they produce lattice defects along their trajectories. High-energy ions, such as cosmic rays, can produce tracks deeper into the grain lattice structure. These lattice defects provide additional conduits that enhance diffusion of volatiles from grain interiors to their surfaces, which in turns enhances desorption processes.

Hydrogen is present in lunar soil samples that have been exposed to the solar wind (DesMarais et al. 1974, Epstein and Taylor 1975, Crider and Vondrak 2003) and is found mostly in the top 500 Angstroms of mature lunar grains (Crider and Vondrak 2003). Solar wind proton bombardment begins with the proton implanting into the surface of a grain where it picks up an electron, producing a hydrogen atom and reducing the molecules in the outer layers of the grain. The reduction (discussed in detail later) produces OH, H₂O, and npFe⁰. It also produces damaged or open atomic bonds, thus creating sites for adsorption of gaseous exospheric molecules (such as H₂O). Hydrogen content is correlated with soil exposure age and maturity in Apollo samples (DesMarais et al. 1974, Crider and Vondrak 2003); it plateaus

(around 50 – 75 ppm) within very mature, equatorial soils (Morris 1976, Crider and Vondrak 2003), which implies that a steady-state is achieved between H_2 release and H_2 generation in mature regolith (Crider and Vondrak 2003).

While ion implantation generates H_2 in soils, H_2 is released via several mechanisms, including diffusion, sputtering, and vaporization. The diffusion rate for lunar soils is thought to be small, thus the release of hydrogen is dominated by sputtering and vaporization. Vaporization of hydrogen occurs predominately during the micrometeoroid impact process, discussed earlier. A steady-state H_2 soil content, therefore, is achieved through a balance of generation and release process rates. This steady state is commensurate with the recent hydroxyl and water signatures detected over the lunar surface (Vilas et al. 2008, Clark 2009, Pieters et al. 2009, Sunshine et al. 2009). Extrapolations to Mercury has several caveats. Dayside temperatures at Mercury are much higher than at the Moon, making thermal desorption of implanted ions more efficient. Regolith porosities and the fraction of fine-grained material influences the relative efficiencies of removal and trapping of ions. Bombardment studies indicate a higher fine fraction on Mercury, thus calculations of the relative retention rates will need to factor these differences.

Physical sputtering

The collision of energetic solar wind or magnetospheric ions with surface grains can release particles via momentum transfer. Such physical sputtering, is a surface effect, acting on the top-most atomic layers. Physical sputtering can release any species, so that elements in the steady-state exosphere reflect surface composition on an atomic level (Johnson et al. 2002; Killen et al. 2007; Wurz et al. 2010), though not in relative abundances. Several studies (Killen et al. 2007; Wurz et al. 2007, 2010) compare expected exospheric compositions due to physical sputtering, photon-stimulated desorption (PSD), and impact vaporization with measured density and spatial distribution within the exosphere. As for the material remaining on the surface, preferential sputtering of elements with high sputtering yields (H, O, and OH for example) will enhance elements of low sputtering yield (Fe and Ti, for example) in the top-most atomic layers (Killen et al. 2007). It has been proposed that physical sputtering reduces and disorders the top-most mono-layers, thus producing amorphous rims (e.g. Hapke 2001). Reduction of Fe^{2+} in iron-bearing grains by physical sputtering produces $npFe^0$, the dominant cause of space weathering.

The rate at which sputtering modifies surface grains depends on:

- § Surface composition

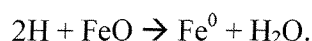
- § Gardening rates
- § Diffusion rates
- § Composition and velocity of impacting ion species (properties of the solar wind)
- § Flux of ions to the surface (presence of a magnetic field)

Wurz et al. (2010), using certain assumptions for Mercury's surface composition calculated a global sputtering rate comparable with the lunar rate. Comparisons with Na exosphere observations and calculations of the diffusive flux of sodium from grain interiors to surfaces show that the sodium exosphere could be sustained by calculated sputtering yields and gardening rates even if all injected sodium were immediately lost to the system (Killen et al. 2007, 2004b). Thus ion sputtering could efficiently remove high-sputtering yield elements (such as H, O, and Na) from the surface, leaving behind a reduced surface enhanced in low-sputtering yield elements (such as Fe and Ti).

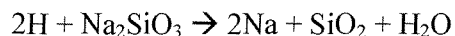
Chemical sputtering

Chemical sputtering releases atoms and molecules from regolith grains due to chemical reactions between implanted solar wind or magnetospheric ions (predominantly implanted protons) with the regolith. It may produce and remove sodium (Potter 1995), hydrogen, hydroxyl, and water (e.g. Crider and Vondrak 2003) from the surface to the exosphere (where they can then be lost through photo-ionization or Jeans escape). Laboratory experiments have shown that proton bombardment of oxides readily forms hydroxyl (Zeller et al. 1996, Gruen et al. 1976, Siskind et al. 1977), which enables chemical sputtering of hydroxyl and water (Crider and Vondrak 2003). The chemical sputtering of hydrogen molecules (H_2) occurs through grain-catalyzed reactions (Duley and Williams 1993). Johnson and Baragiola (1991) predict the sputtering yields of water by solar wind protons to be ~ 0.01 molecule/ion for the Moon. Solar proton flux at Mercury (discussed in detail later) is an order of magnitude higher, implying a similar increase in water production at Mercury.

Solar wind irradiation, in conjunction with micrometeoroid bombardment, is can produce single-domain $npFe^0$ by the following reaction within the impact melt that later forms agglutinates and grain patinas:



Potter (1995) proposed the production of sodium and water by proton sputtering of sodium-bearing silicates through the following reaction:



In this reaction twice as much sodium as water is produced. Potter (1995) argued that Mercury's surface temperatures are optimal for this reaction. The OH radical also serves to reduce any Fe^{2+} to Fe^0 , thereby removing O^{2-} from surface lattice sites (Huguenin 1976, Killen and Ip 1999) and thus helping to produce npFe^0 in the uppermost layers of regolith grains,

Apollo lunar samples included rocks composed of anhydrous minerals (Papike et al. 1991). However, recent reflectance observations of the Moon have shown that hydroxyl and water are ubiquitous within the lunar soil, but have a clear signature of production via solar wind interactions (Vilas et al. 2008, Clark 2009, Pieters et al. 2009, Sunshine et al. 2009). Due to significantly higher temperatures on Mercury it is not clear if similar OH and H_2O production is sufficiently long-lived to produce such signatures.

Alkali earth metals can be both physically and chemically sputtered. Björkas et al. (2009) show in the laboratory that Be can be chemically sputtered by deuterium bombardment, which has implications for other alkali earth metals (such as Mg and Ca). During MESSENGER's third flyby, Mg was detected in the exosphere for the first time (McClintock et al. 2009); Ca was found during the second and third flybys (McClintock et al. 2008, 2009). Production of exospheric Mg and Ca via both physical and chemical sputtering mechanisms needs to be modeled and compared with the observations.

Desorption induced by electronic transitions (DIET)

Desorption induced by electronic transitions (DIET) is a known surface physics phenomenon. The electronic excitation can result from the interaction of electrons (electron-stimulated desorption, ESD) or photons (photon-stimulated desorption, PSD). Both ESD and PSD lead to the desorption (removal from bulk composition to a gaseous or liquid phase) of atoms, molecules, and ions from a surface grain via electronic excitations. These can be band gap excitation, valence/shallow core excitation, or core excitation. In the case of ESD, the electronic excitations are typically generated via the inelastic scattering of low-energy electrons ($\sim 4\text{-}50$ eV) created by higher-energy incident radiation. The localization of these complicated multi-electron excitations at the surface occurs mostly at defects and leads to ESD. Generally, PSD refers to non-thermal desorption events that result from direct single-electron transitions to repulsive excited states. These transitions are mediated by Franck-Condon overlap integrals and involve either visible or ultraviolet photon radiation. PSD can also involve higher-energy photons, such as X-rays which penetrate to greater depths in the regolith. In the case of X-ray interactions, PSD involves core level atomic transitions.

The fractions of neutrals vs. ions desorbed by DIET depend on the incident energy and chemical state of the target. For example, the yield of neutrals typically dominates the ion yields by several orders of magnitude for adsorbates on metallic surfaces and for lower-energy (sub band-gap) excitations. For excitation energies that can Auger decay (A two-electron process where a bounded electron transitions from a less bound shell to a vacant, more tightly bound shell. The energy released in this transition is transferred to a second bound electron, which escapes the atom.), the ion yields can begin to become appreciable, such as for oxides (i.e wide band-gap materials) and mineral surfaces.

Fig. 6 exemplifies a simple one-electron transition for desorption of neutrals via DIET, whereas Fig. 7 shows a more complicated multi-electron process involving Auger decay and Coloumb explosions. In the simpler case, the incident photon or electron induces a charge transfer of an electron trapped in a silicate lattice to an adsorbed species, in this case Na^+ . This neutralizes the Na and places it on a repulsive potential with respect to bonding to the surface. The Na then desorbs with a nonthermal velocity distribution. The Auger stimulated process is more complicated and involves several electronic transitions. The first is the removal of an electron from a shallow core hole, which is then filled by Auger cascading. The energy gained ejects an electron from a nearby site and reverses the Madelung potential. Ions are then ejected with relatively high kinetic energies due to the Coulomb explosion. ESD ion yields can range between 10^{-4} to 10^{-6} per electron at 100 eV.

Stimulated desorption cross-sections vary between neutrals and ions, with cross-sections of $10^{-18} - 10^{-20} \text{ cm}^2$ and $10^{-19} - 10^{-23} \text{ cm}^2$, respectively. Typical gas-phase dissociative ionization cross-sections are 10^{-18} cm^2 at 100 eV. Threshold energies also vary between neutrals and ions. For example, the threshold energy for a one-electron valence level excitation in a neutral is $\sim 5 \text{ eV}$, whereas a shallow core-excitation in an ion is $> 15 \text{ eV}$. Lifetimes also vary between core-hole (10^{-16} s) and valence level ($10^{-15} - 10^{-14} \text{ s}$) transitions. Kinetic energies for neutrals and ions are $< 1 \text{ eV}$ and $1 - 10 \text{ eV}$, respectively. A key issue in DIET is ‘localization’ or self-trapping of energy. This occurs best at defects, thus DIET is very sensitive to defect density. This means that amorphous and radiated samples (where lattice defects are more abundant) typical of regolith materials will tend to have higher DIET cross-sections relative to single crystalline defect-free materials.

DIET processes relevant to Mercury have been evaluated through laboratory simulations and exospheric measurements. They should vary with solar activity, surface temperature, orbital position (apoherm vs periherm), and with the physical characteristics of the regolith, such as porosity, which affects how desorbed materials stick to adjacent surface

grains. The efficiency of ESD is affected by the interactions between the solar wind electrons and Mercury's intrinsic magnetic field (discussed below).

PSD may be the dominant mechanism producing Mercury's sodium exosphere (Mouawad et al. 2011; Burger et al. 2010). Burger et al. (2010) argue that ion sputtering did not significantly contribute to exospheric sodium during these MESSENGER's first two flybys, but that ion bombardment did contribute to the PSD process at high latitudes by enhancing diffusion. PSD, therefore, is a key process modifying the dayside regolith. DIET processes can not only deplete minerals of alkali content, but can remove most atoms and molecules from terminal sites within the lattice structure. These processes remove both oxygen and hydrogen, leaving behind metals like Fe and Mg, sometimes in a reduced state. Neutral species are the dominant ejecta via PSD (Killen and Ip 1999), but refractory species are not affected (Killen et al. 2007).

Modeling by Lammer et al. (2003) has shown latitudinal and orbital dependencies on PSD yields. Sodium yields are greatest at equatorial latitudes during periherm and are 3 times lower at the equator at apoherm. The removal of alkalis from the surface by PSD is tied to the ultraviolet flux. The UV flux can increase ~100 times from low solar activity states to active solar periods or during solar flares (Killen et al. 2007), indicating that the effectiveness of this process is highly time dependent.

Thermal Desorption

Thermal desorption is the removal of adsorbates via heating, and involves volume diffusion from grain interiors to surfaces, surface diffusion between sites with different desorption energies, and electronic excitation and de-excitation (Killen et al. 2007). Thermal desorption rate is governed by diffusion, grain size, and grain lifetime at the regolith surface (Killen et al. 2004b, 2007). Smaller grains diffuse atoms to the surface more quickly than larger grains and are depleted in volatiles more quickly (Killen et al. 2004b) while also serving as a more efficient repository for adsorption of volatiles due to their larger surface to volume ratio.

Leblanc and Johnson (2003) argue that thermal desorption rapidly depletes most of Mercury's sunlit surface of adsorbed atoms, but do not consider resupply by diffusion in their calculations. Over geologic time scales equatorial regions are depleted in adsorbed alkalis, which either migrate poleward (Killen and Morgan 1993a, Killen et al. 2007) or to temporary nightside cold traps, thus replenishing the surface. Also some desorbed alkalis are ionized and removed from the system by the solar wind. As with all processes, thermal desorption

works in conjunction with the other processes acting within the Mercury surface-exosphere-environment system. Thermal desorption is enhanced by lattice defects created during solar wind irradiation. Regolith gardening governs grain exposure time to the surface, thus controlling the volatile depletion rate. As discussed previously, the gardening of Mercury's surface is more efficient than the Moon's, but no quantitative comparisons of grain surface lifetimes have been published.

Transport of materials: The regolith as a sink

The exosphere can be thought of as a transition zone between the upper regolith and loss of material to space. The cumulative effects can be understood by examining lunar samples and measures of the lunar exosphere. Lunar regolith grains reveal evidence for volatile loss through compositional gradients and isotopic ratios. For example, the volatile metal mercury (Hg) was measured in Apollo 11, 12, 14 and 15 samples and Luna 16 core and trench samples (e.g. Jovanovic and Reed, 1972; 1979). The Hg compositional gradients indicate diffusive loss from the soil and repeated resurfacing events. The sequestration of Hg as a polar condensate was predicted to be as high as 0.25 wt% in cold traps (Reed, 1999). The cold-trapping of Hg was confirmed by the observations of Hg in the impact vapor of the LCROSS impact (Gladstone et al., 2010). Quantifying the amount of Hg in the polar traps constrains models of cold trapping efficiencies at the lunar poles. The mass mixing ratio of Hg in the vapor plume measured by the LAMP instrument following the LCROSS impact into Cabeus crater was reported to be 1.2% (Gladstone et al., 2010), five times predicted values for permanently shaded lunar soils (Reed 1999). The cold trap area may in fact be smaller than the 3700 km² assumed by Reed (1999), or, more probably, the extremely volatile species were preferentially measured.

This evidence for lunar cold-trapping has its implications for cold-trapping of volatiles on Mercury. Many of the processes that remove volatiles (including alkalis) have been argued to be more efficient at Mercury compared with the Moon thus placing more material in motion. Once these materials are removed from the surface to the exosphere two paths are possible for their final deposition. Neutrals will either be redirected back to the surface or lost through ionization or photo-dissociation. If redirected to the surface they are either injected near their ejection region or migrate poleward to be trapped in permanent or semi-permanent cold traps. Ions can be recycled to Mercury's surface by gyromotion within its magnetic field (a mechanism not available at the Moon or removed from the system by being picked up in the solar wind and lost downstream. A steady-state between removal from and redeposition

into the surface depends on process rates, regolith porosity (mean free path of ejected material), and gardening rates.

Laboratory Simulations

Laboratory simulations of space weathering processes have been conducted to examine micrometeoroid bombardment, DIET processes, and thermal desorption effects on mineral regoliths.

The micrometeoroid bombardment of asteroid surfaces has been simulated using pulsed lasers on powdered silicates (e.g., orthopyroxene, clinopyroxene, and olivine). These experiments examine how vapor-deposited reduced npFe^0 affects UV-VIS-NIR spectra and provide clues to space-weathering rates, but there have been issues. Laser irradiation effects depend on energy flux (J/cm^2) of the single pulse, pulse duration, and wavelength of the beam (e.g., Chrisey and Hubler Eds., 1994). Fluence determines which of two energy regimes the experiment is simulating. At low flux, laser irradiation induces mainly thermal and chemical effects. At higher flux, laser-light intensity can induce vaporization, depending on target properties and laser parameters. With silicate samples, which have strong-to-medium laser absorption, the threshold fluence for nanosecond pulsed laser is typically between 0.5 and 2 J/cm^2 per pulse (Bauerle, 2000).

The first laser space weathering experiments performed on ordinary chondrites used microsecond pulsed laser irradiation to redden and darken reflectance spectra (Moroz et al., 1996). The pulse duration in these experiments was much longer than micrometeoroid (1–10 μm size) impact time scales so the observed spectral changes may have resulted from glass formation (Sasaki et al. 2001). Shorter pulse durations (6–8 ns) were employed by Yamada et al. (1999), Sasaki et al. (2001, 2003), and Hiroi and Sasaki (2001) using a nanosecond pulsed Nd:YAG infrared laser ($\lambda = 1064 \text{ nm}$) on pressed silicate powder pellets. They showed progressive darkening and reddening of UV–VIS–NIR silicate spectra with increasing shot number attributed to formation of coatings enriched in vapor-deposited npFe^0 (Sasaki et al., 2001).

Brunetto et al. (2006) noted an issue with infrared lasers is that changes in target material optical properties were the result of surface damage and stresses induced by thermalization from the incident infrared beam. In contrast, an ultraviolet laser causes direct molecular bond breaking and ablation to occur, and rapid heating and cooling rates produces less surface damage to materials. Experiments by Brunetto et al. (2006) using a nanosecond pulsed UV ($\lambda = 193$ and 248 nm) excimer laser on pressed silicate powder pellets produced,

on an energy dose comparable to a time of 10^8 years at 1 AU, higher spectral slopes than Sasaki et al. (2001) by a factor of $\sim 50\%$, suggesting that UV excimer lasers are more efficient than infrared lasers at reddening silicate samples.

Space weathering process effects are dependent on surface composition. Laboratory simulations of micrometeoroid bombardment in low-iron materials shows variations in spectral alterations dependent on composition (Sasaki et al. 2002, Marchi et al. 2005). Sasaki et al. (2002) irradiated samples of low-iron olivine and pyroxene and found that spectral changes were more pronounced in the olivine samples. Similarly, Marchi et al. (2005) irradiated iron-poor olivine and orthopyroxene to examine ion-sputtering-induced spectral changes and also found larger spectral changes in the olivine samples.

Currently it is not clear whether UV excimer or near-infrared laser irradiation most closely simulates micrometeoroid space-weathering. It is possible one laser type replicates Mercury's micrometeoroid process while the other matches micrometeoroid weathering on asteroids, as melting will vary depending on impact parameters. For instance, near-infrared laser experiments that produce relatively high degrees of melting by thermalization could be more relevant to micrometeoroid weathering on Mercury, while UV laser simulation, with its lower melt production, might be more relevant for asteroids.

Laboratory analyses of DIET processes have typically focused individually on ESD or PSD, though they have many similarities. Yakshinskiy and Madey (2000) have shown that both ESD and PSD have threshold energies of ~ 4 eV and the desorbing atoms are 'hot' with suprathermal velocities. For example, PSD desorbed sodium is suprathermal with a peak speed of ~ 900 m/s and a velocity distribution best described by a Weibull function (Yakshinskiy and Madey 2004).

Simulations of ESD have been conducted primarily on amorphous SiO_2 films (Yakshinskiy and Madey, 2000, 2003, 2004, 2005), Na- and K-bearing glasses (McLain et al. 2010), and lunar basalts over which a Na monolayer has been deposited (Yakshinskiy and Madey 2003, 2004, 2005). These experiments have shown temperature dependencies to DIET yields. DIET desorption of Na was shown to increase tenfold from 100 to 470K (Yakshinskiy and Madey 2004). Yakshinskiy and Madey (2005) observed a reversible temperature dependence of ESD desorbed Na from lunar basalt. Experimental ion yields display slight temperature dependencies between 150 – 350K, however these ion yields show linear increases with temperature between 350 – 550K (McLain et al. 2010). Above 400K the ion yields from the samples show temperature dependencies that are reversible and reproducible (McLain et al. 2010). These temperature dependencies have been attributed to thermally-

induced changes in grain surface bonding sites (Yakshinskiy and Madey 2004). Changes in density and the location of defect sites, in which thermal changes induce local atomic coordination site changes, enhance the ESD process and can explain the reversible temperature dependence seen in experimental desorption yields (Yakshinskiy and Madey 2004, McLain et al. 2010). This is also consistent with lattice expansion, increased hole localization within surface defects, and the diffusion of defects or vacancies to the grain surface (Chen et al. 2005, McLain et al. 2010).

Desorption yields from films, however, differ from yields within regolith due to increased sticking probabilities within a porous, multi-grained medium. Measurements of Na and K sticking probabilities show K has a nearly constant sticking probability over 100 – 500K, whereas Na displays a decreasing sticking probability with increasing temperature over this temperature range (Yakshinskiy and Madey 2005). DIET desorption yields are therefore species dependent. Table 1, extracted from McLain et al.'s (2010) experimental results of show threshold energies for the desorption of various ionic species from Na- and K-bearing glasses.

Table 1. Desorption threshold energies from Na- and K-bearing glasses

Specie:	H ⁺	H ₂ ⁺	O ⁺	H ₃ O ⁺	Na ⁺	K ⁺	O ₂ ⁺
Threshold energy (eV)	25±2	40±2	30±2	40±2	30±2	30±2	90±2

ESD experiment results were combined with electron (e⁻) precipitation simulations to predict ion outflow off Mercury's surface. Using solar wind conditions from MESSENGER's first two Mercury flybys, and integrating over the entire planet, simulations indicate ~ 10²⁶ e⁻/s impact Mercury's surface (Schrivver et al. 2010). Combined with laboratory ESD ion yields of 10⁻³ – 10⁻⁵ ions/e⁻ (with the range depending on the impinging electron energy for 200 eV – 2 keV) gives a value of 10²¹ – 10²³ ions/s emitted from Mercury (McLain et al. 2010; Schrivver et al. 2010). This is comparable to estimated ion sputtered outflow yields ranging between 6.0 × 10²¹ – 3.8 × 10²⁴ s⁻¹ (Killen et al., 2004).

Thermal desorption has been studied using SiO₂ (Madey et al. 1998) and Al₂O₃ (Shao and Paul 1993) films coated with mono-layers of sodium. Laboratory measures show desorption yields are related to both temperature and sodium layer thickness (Madey et al. 1998). Fractional mono-layers desorb at appreciable rates for temperatures greater than 500 –

600 K, whereas multi-layers desorb at much lower temperatures with a peak near 350 K (Madey et al. 1998, Killen and Ip 1999). The desorption temperature from Al_2O_3 surfaces ranges from 300 – 400 K for both fractional and multi-layers of sodium (Shao and Paul 1993, Killen and Ip 1999).

Rates of thermal desorption from metal oxide surfaces will depend on the composition of the minerals and the presence of other atoms in low concentrations (Killen et al. 2007). For example, the thermal desorption energy for potassium from the same type of mineral can range between 0.83 – 2.35 eV by the inclusion of 2 wt% of Mn (Kotarba et al. 2004, Killen et al. 2007). Studies suggest that the desorption energy of alkali atoms from oxide minerals is ~ 2 eV or greater (Holmlid 2006, Killen et al. 2007). These experiments indicate that thermal desorption rates will vary between the Moon, Mercury, and asteroids based on compositional differences in addition to temperature.

Process summary

Based on theoretical, laboratory, and lunar sample studies in conjunction with remote observations, the affects of the various exosphere-environment-surface processes on Mercury can be assessed. Micrometeoroid bombardment involves gardening, melt and vapor production, and is influenced by preferential processing. Solar radiation processes depend on many criteria (such as grain diffusion rates, solar wind and interplanetary magnetic field characteristics, and flux to the surface), some of them regolith properties controlled by impact processes (such as gardening rates, regolith grain size and porosity). This section summarizes the conclusions from the process discussion of the previous sections.

Theoretical studies (Cintala 1992, Borin et al. 2009) based on impact experiments suggest Mercury's regolith is overturned more quickly than the lunar regolith; implying regolith grains are exposed at the surface for shorter periods of time, but are exposed more often. This is based on impact excavation volumes being slightly elevated and impactor flux being much higher on Mercury than the Moon. The accumulated time a grain spends at the surface, exposed to the space environment is unknown.

Accumulated exposure time affects all surface maturation process rates. For example, asteroids (especially smaller ones) have a net loss of material due to impacts so that processed regolith is gradually replaced by fresh substrate material. On the Moon and Mercury, however, the same surficial regolith material is repeatedly bombarded, churned, and subjected to space weathering processes.

Impacts on Mercury produce an order of magnitude or more impact melt and vapor compared to on the Moon, implying a larger component of impact glasses and agglutinates within Mercury's regolith. Conversely, asteroids contain much less melt and vapor products compared to either the Moon or Mercury. This larger reservoir of vapor to coat adjacent grains implies the potential to form thicker rims on Mercury soil grains. Rim thickness, however, will be governed by the accumulated surface residence time, which is currently unknown.

The rims of regolith grains, especially the outer most few mono-layers, are also processed by solar radiation. These processes depend primarily on solar wind properties and solar flux (ions and photons) to the surface. Solar wind properties, such as composition and velocity, are assumed to be similar between Mercury, the Moon, and the main belt. The surface flux varies due to solar distance and Mercury's magnetic field (a more in-depth discussion of the solar wind and magnetic field properties is provided in the following sections). For comparative purposes at this point in the discussion it is assumed the solar wind has access to Mercury's surface. The validity and impact of this assumption is examined in the next section. The solar radiation processes include ion implantation, sputtering, DIET, and thermal desorption.

Ion implantation introduces ions into the grain's atomic lattice structure, and creates lattice defects. Lattice defects enhance diffusion of material from the grain interior to the grain surface, and creates radiation damaged, amorphous rims on grain surfaces. These effects contribute to a reducing environment and the production of npFe^0 , OH, and H_2O .

The sputtering processes (both physical and chemical) preferentially remove lighter materials (H, O, and OH), thereby reducing the top mono-layers of surface grains. Laboratory measures show sputtering also removes alkali species. Sputtering, therefore, contributes to creating amorphous rims on exposed grain surfaces and depletes the top mono-layers of alkalis. The removal of material via sputtering is balanced by trapping of material by nearby, adjacent grains. The trapping efficiency is governed by surface temperature, regolith porosity, and regolith grain sizes.

DIET processes work similarly to the sputtering processes by removing elements from the top mono-layers of exposed surface grains. Laboratory studies indicate that thermal desorption and PSD are more efficient at removing volatiles (including alkalis) from warmer surfaces, resulting in a surface that more depleted in volatiles and alkalis on Mercury compared with the Moon or main-belt asteroids.

All processes will be affected by diffusion rates and surface composition. Diffusion rates, in turn, depend on composition, temperature, and solar wind exposure (radiation damage

enhances diffusion rates). Diffusion rates at Mercury and the Moon differ due to different thermal environments and precipitating plasma energies. Although the solar wind has the same mean energy at Mercury and the Moon, protons are accelerated when they cross Mercury's cusp region (Masetti et al., 2007). Typical solar wind impacts the Moon with energies of ~ 1 keV. At Mercury impacting protons have energies of $\sim 3 - 7$ keV. Using lunar exospheric measurements, an energy dependence for Na diffusion is observed: when the Moon crosses magnetospheric plasma sheet ions (~ 3 keV), the sodium exosphere is enhanced over occurrences where the Moon passes through the Earth's magnetosphere but misses the its current sheet. The effect is attributed to enhanced grain diffusion due to vacancies created radiation by more energetic plasma (Sarantos et al. 2008; Sarantos et al. 2010). By extrapolation, diffusion is expected to be more enhanced at Mercury because the plasma precipitating onto the surface is more energetic.

Composition is also a component in assessing relative process rates and efficiencies. For example, the rates and depths a surface is comminuted is compositionally dependent; a feldspathic surface breakdowns more rapidly than a pyroxene rich surface. This influences the regolith grain size distribution and the percentage contained in the finer (< 45 μm) size fraction (which governs the reflectance properties). Small grains diffuse material from their interior to their surface more rapidly. Due to their larger surface to volume ratio, however, they also adsorb atoms and molecules more effectively than larger grains, thus functioning as a repository for exospheric species. The percentage of smaller, finer grains within a regolith influences the source versus sink properties of the surface. The balance between these and the relationship with grain size distribution is not well known.

Differential melting of material, which can explain many of the lunar sample characteristics, is key to understanding melt and vapor contributions. A melting sequence of glass $>$ plagioclase (feldspar) $>$ pyroxene $>$ ilmenite (with glass melting preferentially) has been demonstrated by Pieters and Taylor (2003). Modeling of impact melt and vapor production on Mercury relative to the Moon has not factored in such possibilities as Mercury's regolith being richer in oxides, such as ilmenite, thus potentially reducing the current estimates of melt and vapor production. The magnitude of this reduction is unknown.

Each process presented works to provide a reducing environment, key to the production of npFe^0 . The production of npFe^0 (the leading contributor to the optical effects of space weathering) depends on the presence of iron within the regolith. The relative process rates and efficiencies point to a greater abundance of npFe^0 on Mercury than on the Moon, assuming a similar surface iron content, which has not been established. Flyby measurements from

MESSENGER's neutron spectrometer have been interpreted to indicate an iron content similar to some lunar highlands (Lawrence et al. 2010), however, spectral observations indicate that ferrous iron is not present in silicate form above the 2 wt.% level (McClintock et al. 2008). Theoretical modeling studies are commensurate with an iron content mostly converted to npFe^0 of various size fractions (Lucey and Riner 2011).

Composition variations are also a key component in comparisons with asteroids, whose surface mineralogical composition is different from both the Moon and Mercury. While iron is present in silicates on the Moon, iron on Mercury may reside in metal oxides (such as ilmenite, Denevi et al., 2009; Riner et al. 2010). Iron is abundant in ordinary chondrites as both metal and cations within the mineral complex. Achondritic minerals, like those on the surface of Vesta, do not contain a metal iron component and appear less space-weathered than main-belt asteroids of ordinary chondritic composition. Olivine grains are especially susceptible to space weathering whereas opaque minerals are not (Sasaki et al. 2002, Marchi et al 2005). Studies (Pieters et al. 2000, Hapke 2001, Noble et al. 2004) show, however, that even modest creation of nano-phase iron on the surfaces of main-belt asteroids is sufficient to produce the very significant optical changes that are observed.

The Environment

The Mercury and lunar environment have many generic similarities, from exposure to solar wind and radiation to meteoritic impactors. The important factors affecting the surface weathering processes include variations in flux, velocity, and composition of the interacting materials. A major difference between these two bodies is Mercury's internally generated magnetic field, which influences the solar wind surface interactions, creating important differences in the weathering process effects between Mercury and the Moon.

This section explores Mercury's environment by examining:

- § the character of the micrometeoroid population,
- § the effects of electric charging of the regolith,
- § the character of the solar wind and its population of particles,
- § the nature of Mercury's magnetic field and its shielding of the surface, and
- § the solar radiation flux including surface temperature effects.

The following subsections compare Mercury's environment with the lunar and asteroid environments to evaluate the relative importance and process efficiencies.

Micrometeoroid population

The major sources of the inner solar system micrometeoroid population are asteroids and comets. Understanding of the micrometeoroid population comes from dust measurements acquired at Earth orbit (1 AU). The best estimates of the spatial distribution of dust between 1 and 0.1 AU come from the extrapolation of 1 AU measurements. This assumes radial dependencies of $r^{-1.0}$ and $r^{-1.5}$ for the number density and flux, respectively (Mann et al. 2004).

Production mechanisms of interplanetary dust within 1 AU includes Poynting-Robertson deceleration of material originating beyond of 1 AU, fragmentation due to collision between interplanetary grains, and materials released from comets (Mann et al. 2004). Micrometeorite dust removal occurs via dust collision fragmentation, sublimation, radiation pressure acceleration, and sputtering (Mann et al. 2004). Modeling indicates that collisions change the size distribution of interplanetary grains inward of 1 AU (Mann et al. 2004). The composition of the interplanetary grains as a function of heliocentric distance is not known. Composition and grain size distributions are assumed to be similar between Mercury and the Moon for the comparative discussions in this paper.

Studies of nanometer scale size particles indicate the flux of these particles exceeds that of micrometer-sized dust by at least two orders of magnitude (Czechowski and Mann 2010, Kaiser et al. 2007). The speed of these nano-particles can reach solar wind speeds (~ 300 km/s) at 1 AU.

Electrostatic charging and dust levitation

Observations and theoretical studies of electrostatically transported dust above the lunar terminator show submicron-sized grains can be levitated and transported tens of kilometers in altitude (e.g. Criswell 1973, McCoy and Criswell 1974, Rennilson et al. 1974, Zook and McCoy 1991, Halekas et al. 2002, Stubbs et al. 2006, Colwell et al. 2007). The lunar surface is electrostatically charged by the photoemission of electrons due to solar ultraviolet (UV), X-rays, and interactions with the local plasma environment (Manka 1973). Similarly charged grains are then levitated through repulsive forces.

Excitation of the dayside by solar UV and X-rays causes the photoemission of electrons from the surface grains, creating a positive potential on the dayside (Farell et al. 2007). Dust is also charged by electron and ion impacts, but this is a more complex process (e.g Abbas et al. 2010). Incident electrons sticking to a dust grain charge it negatively, however the emission of secondary electrons will charge it positively. Experimental studies by

Abbas et al. (2010) show that charging of dust by electron impact depends on grain size, surface potential, and composition, and electron energy and flux. On the lunar night side low-density electron plasma current interactions negatively charge the surface (Farell et al. 2007), thus levitating negatively charged dust grains. The complex electric field at the terminator (where the surface goes from dayside-positive to nightside-negative) transports and mixes the levitated dust (the finer fraction of the regolith grains).

No intrinsic magnetic field shields the lunar surface from the plasma environment, however, localized areas of magnetized crust have been observed (e.g. Coleman et al. 1972, Russell et al. 1975, Hood et al. 1981). Blewett et al. (2010) show lunar swirls (complex, bright albedo patterns with no associated topographic expression) only appear in regions of local magnetized crust, though not all magnetized regions display swirls (Blewett et al. 2010). Based on these correlations and measures of soil maturity indices Blewett et al. (2010) narrow plausible swirl formation mechanisms to:

- § Shielding of the surface from solar wind ion bombardment by the magnetic anomaly resulting in a less space weathered regolith (Hood and Schubert 1980, Hood and Williams 1989)
- § Preferential accumulation of fine-grained, feldspar-rich dust by electrostatic levitation induced by solar wind interactions with the local magnetic anomaly (Garrick-Bethell et al. 2009a, 2011)

If the first process dominates lunar swirl formation, this implies that solar wind ion bombardment is the main lunar space weathering process (Blewett et al. 2010). If the second process dominates, then electrostatic levitation contributes measurably to regolith mixing of the finer soil fraction.

The case for Mercury is more complex. Electrostatic levitation of dust grains by photoemission on the dayside can be expected. With the increased solar flux at Mercury compared with the Moon, it can be hypothesized that Mercury's surface will be more highly charged, perhaps levitating material to greater altitudes. On the nightside Mercury's intrinsic magnetic field will moderate the creation of plasma electron currents, though it has been shown in the MESSENGER plasma and magnetic field measurements that reconnection events expose the nightside to electrons in the magnetotail (Slavin et al. 2009, 2010a, 2010b; see section below for discussion). Study of the MESSENGER flyby images of Mercury has not discovered albedo markings similar to lunar swirls (Blewett et al. 2010). To date no local

regions of magnetized crust have been detected (Purucker et al., 2009), although isolating the internal magnetic field is difficult and flyby coverage from MESSENGER was limited.

Electrostatic levitation works to globally mix the finer regolith fraction (which dominates the optical properties). A proposed example of this contribution to global mixing is seen in lunar highland soil samples. Apollo 16 highland agglutinitic glass is enriched in mafic components compared to the bulk soil composition. Taylor et al. (2010) suggest this is due to the selective addition of a mare glass component. They argue that this selective addition is accomplished via ballistic transport (where the finer, agglutinitic fraction is transported farther by impact processes) and electrostatic levitation of the finer fraction (Farell et al. 2008). The differential melting sequence (glass > plagioclase > pyroxene > ilmenite), which includes the preferential melting of mafic-rich (mare composition) glass over Al-rich (highland composition) glass (Taylor et al. 2001a, 2001b, 2003) creates the enrichment in mafic material in highland agglutinates (Taylor et al. 2010). The implications for Mercury are uncertain, but could contribute to a more globally mixed finer fraction.

The solar particle environment

The solar wind, a continuous flow of charged particles (mostly protons and electrons), streams radially from the Sun to the heliosphere (a void in the interstellar medium structure created by the solar wind and the frozen-in magnetic field). This section examines solar wind properties in order to relate them to the exosphere generation – surface maturation processes.

General Properties

Mercury is engulfed in a stream of particles originating from the Sun. The space environment at 1 AU is described in Fig. 8, where O fluxes (left-hand side) are propagated to compute H fluxes at Mercury's orbit (on right-hand side) using simple scaling laws. Solar wind as well as micrometeoroid impacts contribute to Mercury's exospheric density (Wurz et al., 2010, and references therein). The relative contribution to surface alteration by the various radiation processes is highly dependent on the solar wind dynamic pressure and interplanetary magnetic field (IMF) (Wurz and Lammer, 2003).

The physical sources, identified in Fig. 8, of the incident particles are segregated in terms of energy. Energies ranging up to 5 keV/nucleon are dominated by solar wind, the expanding corona nominally consisting of a quasi-neutral plasma of ~ 96% protons (H^+) and electrons, as well as ~4% alpha particles (He^{2+}) and <0.1% of heavy ions (von Steiger et al., 2000). At the highest energies (>1 GeV/nucleon) are galactic cosmic rays (GCRs) that enter

the heliosphere from astrophysical sources and interact with the solar wind's turbulent magnetic field. The anomalous cosmic rays (ACRs) are particles thought to be of heliospheric origin and accelerated in the boundary regions of the heliosphere. They are observable near solar minimum when reduced modulation effects allow them to enter into the heliosphere. Particles of energy intermediate to these populations are generally referred to as suprathermal particles or energetic particles. They originate from transient acceleration in the heliosphere, or from nearly ubiquitous acceleration within the solar wind.

This section examines the solar wind particle populations and their time-dependent changes.

Solar Wind Plasma: Solar wind plasma escapes from the solar corona and expands supersonically into the heliosphere at speeds of 400-800 km/s and at a density of $\sim 10/R^2 \text{ cm}^{-3}$, where R denotes the heliospheric distance. Solar wind acceleration occurs within 0.1 AU. In situ measurements of the solar wind bulk properties, e.g., density, velocity, and composition, reveal two main types of quasi-stationary wind, fast (600-800 km/s) and slow (<450 km/s) wind. These two solar wind types originate from very different solar environments. Heliospheric dynamic processes modify the speed of propagating plasma (e.g., McComas et al., 2002), thus recent studies de-emphasize the terms “fast” and “slow”, and classify the solar wind by its charge state composition (Geiss et al., 1995; Gloeckler, et al. 2003): solar wind originating in coronal holes versus solar wind originating outside coronal holes. The first originates in cool solar regions with strong concentrations of open magnetic field (coronal holes); the second is associated with topologically closed magnetic field structures in the solar atmosphere (non-coronal hole).

A third category (Zhao et al., 2009) of heliospheric plasma is transient plasma associated with coronal mass ejections (CMEs). Approximately 15% of heliospheric plasma during the solar cycle – mostly during times of elevated solar activity - has a transient character. The relative contributions of coronal hole and non-coronal hole wind depend on the solar cycle. Slow, streamer associated wind dominates the in-ecliptic plasma near Mercury during solar minimum, but coronal hole associated wind becomes common during elevated solar activity at solar maximum.

Important compositional characteristics define these three plasma sources. Coronal hole associated wind has an elemental composition comparable to the solar photosphere (Grevesse and Sauval, 2002). Non-coronal hole wind and CMEs have compositions rich in elements with low (<10 eV) first ionization potential (FIP), for example elevating Fe/O by a factor of 2-4 over photospheric values (Zhao et al., 2009; von Steiger and Geiss, 1993).

Table 2. Mean solar wind properties at Earth and near Mercury

Parameter	Non-Coronal Hole Wind		Coronal Hole Wind	
	1 AU	0.4 AU	1 AU	0.4 AU
n (protons/cm ³)	8.3	74.1	2.7	20.8
v (km/s)	327	348	702	667
T_p (x 10 ⁵ K)	0.34	0.55	2.3	2.8
T_e (x 10 ⁵ K)	1.3	1.9	1.0	1.3
T_α (x 10 ⁵ K)	1.1	1.7	1.4	7.3
LTE C charge state temp (K)	8×10^5		$1.4 - 1.6 \times 10^6$	
O ⁷⁺ /O ⁶⁺	0.2		0.01	
Ave Fe charge state and Temp (K)	11.2 (1.4×10^6)		10.1 (1.2×10^6)	
He/H	0.01		.048	
H/O	2300		1500	
C/O	.67		.68	
Fe/O	.12		.09	
Mg/O	.15		.11	

Properties measured by Helios 1 & 2 and IMP 7/8 (Schwenn, 1990). Ionic charge state ratios and temperatures at 1 AU are from Ipavich et al. (1998), Zurbuchen et al. (2002), and Lepri et al. (2001); elemental abundances at 1 AU are from von Steiger et al. (2000), von Steiger et al. (2010), Bame et al. (1997), and Bochsler (1998). A more complete list can be obtained from these sources.

The solar wind's ionic charge state reflects its origin. For example, coronal-hole solar wind has a substantially lower oxygen charge state ratio ($O^{7+}/O^{6+} = 0.01$) than non-coronal hole wind ($O^{7+}/O^{6+} = 0.2$), and CMEs ($O^{7+}/O^{6+} > 1$) (Zurbuchen et al., 2002; Gloeckler et al., 2003). Solar wind properties at 1 AU are summarized in Table 2, along with some properties near Mercury, as measured by the Helios spacecraft (Marsch et al., 1982; Schwenn, 1990). Model fits to the data from MESSENGER's first flyby of Mercury estimate that the proton speed, density, and temperature were about 450 km/s, 60 cm⁻³, and 10⁵ K, respectively (Baker et al., 2009).

Suprathermal Plasma: The plasma in the suprathermal tail of the solar wind distribution is accelerated to energies ranging from 1 keV/nuc to several MeV/nuc. The cause

of this acceleration is an active area of research, and explanations invoke such phenomena as local compressive turbulence (Fisk and Gloeckler, 2008; Fisk et al., 2010), acceleration by electric fields from solar wind dynamic processes (Drake et al., 2009) or shock acceleration (Jokipii and Lee, 2010), even though this seems unlikely due to the nearly ubiquitous nature of the particles (Zurbuchen et al, 2004).

The importance of these suprathermal particles should not be underestimated. Depending on the orientation of the IMF, portions of the surface are shielded from the solar wind plasma by Mercury's dipole magnetic field (Sarantos et al. 2007, Kabin et al., 2000). That shielding is substantially less efficient for suprathermal particles, which are higher in energy and nearly omni-directional. The suprathermal ion flux expected at Mercury during times of slow solar wind flow is over $10^5 \text{ cm}^{-2} \text{ s}^{-1}$, while solar wind flux is $\sim 3,000$ times greater. The plasma composition in the suprathermal tails of the velocity distribution includes components of the solar wind at 1 AU. At farther radial distances, however, the suprathermal tail plasma is primarily composed of interstellar pickup ions (Fisk and Gloeckler, 2006).

High-energy Particles: Heliospheric plasma with energies above that of the solar wind include high-energy particles ejected from the Sun, such as solar energetic particles (SEPs), and particles that gain energy by acceleration in the heliosphere. High-energy particles propagate almost freely about the heliosphere, making particle fluxes near Mercury highly transient and nearly unpredictable.

SEP events contain plasma with MeV/nucleon energies and are characterized as impulsive (on time scales of minutes to hours) or gradual (hours to days), though the distinction is somewhat arbitrary (Klecker et al., 2006). Impulsive events are flare-associated, containing particles with high charge states indicating temperatures in the $2\text{-}7 \times 10^6 \text{ K}$ range (Luhn et al., 1984). From $\sim 10\text{-}50 \text{ MeV/nuc}$, composition data reveals that Fe-rich impulsive events are primarily accelerated solar flare plasma (Mewaldt et al., 2007). Gradual events, associated with expanding coronal mass ejections, contain plasma characteristic of fast CMEs, and possibly suprathermal particles near the Sun (Reames, 1999; Desai et al., 2006). Their elemental composition does not match the bulk solar wind (Mewaldt et al., 2007; von Steiger et al., 2000).

Particles in the heliosphere can be accelerated by shocks, such as those forming at the edges of corotating interaction regions (CIRs). These shocks are found to contain pickup ions and coronal hole wind (Gloeckler et al., 1994). Such CIRs typically form at heliospheric distances of $>1 \text{ AU}$ and are not expected to be a big factor near Mercury. Helios showed

energetic particle events are highly structured and transient, although they appear merged at larger heliospheric distances.

Cosmic Rays and Anomalous Cosmic Rays. Anomalous cosmic rays (ACRs) are thought to be pickup ions that traveled beyond the termination shock of the solar wind, experienced acceleration, and returned to the heliosphere. The composition of ACRs matches both interstellar and inner source pickup ions (Gloeckler and Geiss, 2001), and their energies range from ~ 10 to 50 MeV/nucleon.

Galactic cosmic rays (GCRs) are mostly protons (86%), alpha particles (8%), and electrons (5%), with trace amounts of heavy ions (Mewaldt, 1994; Evenson et al., 1983). They are detected at 1 AU with energies >10 MeV/nucleon.

Solar wind and Interplanetary Magnetic Field near Mercury

The IMF affects solar wind characteristics and its interaction with Mercury's magnetic field. Visualizations of Helio observations within Mercury's orbit (Figure 9) provide relevant information and insight into Mercury's local space environment (Sarantos et al., 2007). Evident in Fig. 9 is the seasonal variation of the driving forces to Mercury: an average IMF strength, ~ 40 nT around Mercury's perihelion, and a solar wind pressure up to tens of nPa. Given Mercury's location in the inner heliosphere, the magnetosphere is subjected to low Mach numbers flows. This appears to enhance the magnetic reconnection efficiency between the planetary and interplanetary magnetic fields (Slavin and Holzer, 1979), resulting in improved access of plasma to Mercury's surface. The following section describes what is currently understood regarding Mercury's magnetic field, its interactions with the solar wind environment, and its effects on solar wind – surface interactions.

Magnetic field

Large-scale planetary magnetic fields greatly impede solar wind ion access to the surface, thereby reducing weathering process rates such as erosion due to sputtering of regolith-derived exospheric species and solar wind-induced chemical processes in the soil. The effectiveness of magnetic shielding depends on solar wind conditions and the strength of the planetary and interplanetary magnetic fields. Mercury's surface is especially susceptible to solar wind impact owing to its lack of a dense atmosphere, weak internal field, and the strong solar wind and IMF environment. In comparisons with the Moon and asteroids it is important to understand how Mercury's magnetic field affects particle radiation process rates.

Mercury's Field and its Dynamic Magnetosphere

Knowledge of Mercury's magnetic field, discovered during the Mariner 10 flybys in the mid 1970s, has been greatly extended by the three MESSENGER flybys in 2008-2009 (Anderson et al., 2008; 2010; Slavin et al., 2008; 2009; 2010a,b). These observations confirmed Mercury's planetary field is stable over long time scales and is primarily dipolar with a surface field of $\sim 200 - 250 \text{ nT-R}_M^3$ (Anderson et al. 2008; 2010; Alexeev et al., 2010). The weak field by planetary dynamo standards is subjected to such strong forcing (Fig. 9, Sarantos et al, 2007) that it barely stands off the solar wind, forming a dayside magnetosphere that extends, on average, to distances of $\sim 1/3$ of Mercury's radius ($1 \text{ R}_M = 2440 \text{ km}$). This proximity means that at times of high solar wind ram pressure (e.g., interplanetary shocks and CMEs), the magnetopause may be compressed all the way to the surface (e.g., Kabin et al., 2000).

Another mechanism for reducing the magnetospheric obstacle is erosion of the dayside by reconnection. MESSENGER Magnetometer measurements clearly demonstrated Mercury's magnetosphere is extremely variable on timescales of minutes as a result of reconnection of the IMF with the planetary magnetic field (Slavin et al., 2009; 2010a; 2010b). Two forms of variability are: (1) the recurrent presence and spatially extended nature of magnetic Flux Transfer Events (FTEs) under southward IMF at Mercury (Slavin et al., 2008; Slavin et al., 2010a); and (2) the recurrent presence of multiple plasmoids, traveling compression regions, and cycles of loading-unloading in Mercury's magnetotail (Slavin et al., 2010b). The repeated appearance of these periods suggests that a succession of global compressions of the forward magnetosphere and episodes of reconnection in the tail can be produced by the variable north-south IMF B_z component. These observations indicated Mercury's magnetosphere is much more responsive to IMF direction and dominated by the effects of reconnection than that of Earth or other magnetized planets (Slavin et al., 2009; Slavin et al., 2010b).

The consequence of these observed reconnection effects is that Mercury's field is much more permeable by the solar wind. FTEs are episodes of reconnection of the planetary field with the IMF on the dayside magnetopause, during which magnetic flux is transferred from the dayside to the magnetic tail. An average measured FTE diameter at Mercury is $\sim 900 \text{ km}$, ($\sim 0.4 \text{ R}_M$). This size corresponds to 28% of the 1.4 R_M mean distance from the center of the planet to the nose of the magnetopause (Slavin et al., 2009; Slavin et al., 2010a). Such large FTEs significantly disturb the topology of the entire dayside magnetosphere, and thus the flux of solar wind ions reaching the surface. The largest observed FTE had an inferred diameter of

$1 R_M$, and its open magnetic field increased the fraction of the surface exposed to the solar wind by ~ 10 – 20 percent over steady IMF driving (Slavin et al., 2010a). The actual increase in precipitating flux could be much more, given that these perturbations connect the mid-latitude surface to plasma from the densest, most compressed region near the nose of the magnetopause, which was previously thought to be excluded from accessing the surface (e.g., Sarantos et al., 2007). Even greater solar wind impact, especially at low latitudes on the dayside hemisphere, may occur during reconnection-driven cycles of magnetic flux “loading” and “unloading” of the tail, as observed by MESSENGER during its third flyby, when the IMF north-south component was variable (Slavin et al., 2010b). The transfer of magnetic flux into the tail reduces the effective magnetic field obstacle that the solar wind sees on the dayside, therefore increasing accessibility. The tail flux contents at the time of the peak loading events were estimated to be at least 30%, and for the most intense event possibly 100%, of the available magnetic flux from Mercury (Slavin et al., 2010b). Under such extreme conditions, the entire magnetic flux content of the dayside may be pulled back into the tail exposing the equatorial surface to the solar wind for ~ 1 min at a time, and up to 100 % of the shocked solar wind may access the surface. This is followed, during the unloading phase, by intense precipitation of plasma onto Mercury’s nightside minutes later. Just how intense the supply of solar wind ions to the surface may be during active magnetospheric conditions is presently under study.

Interactions of the surface with the Interplanetary Magnetic Field and Solar Wind

Models of solar wind-Mercury interactions, which help elucidate the degree of surface radiation weathering, predict that large portions of the surface are exposed to the solar wind even when active magnetospheric conditions are absent. With such an “open” magnetosphere solar wind ion access to the surface may as effective on Mercury as the Moon.

The steady-state access rate of solar wind ions to Mercury’s mid- and high-latitude surface through the outer boundary of the magnetosphere, (i.e. the magnetopause, and the two magnetic cusps) was estimated by Sarantos et al (2007). The study used 40-min averaged data from the Helios spacecraft to describe Mercury’s solar wind environment, and combined them with a model of Mercury’s magnetosphere to evaluate the present-day solar wind precipitation rate in a statistical sense. It was found that this rate varies from $2 - 4 \times 10^{25}$ ions s^{-1} at aphelion to $8 - 15 \times 10^{25}$ ions s^{-1} at perihelion due to Mercury encountering changing solar wind environments in its eccentric orbit. These estimates, obtained by the assumption of

a Mercury dipole moment of $350 \text{ nT } R_M^3$, are supported by those made by a number of other magnetospheric models (e.g., Kallio and Janhunen, 2002; Massetti et al., 2007).

The region accessible to the solar wind is regulated mainly by the IMF orientation, but the entry of solar wind and the related weathering effects are not confined to high-latitude regions. Large regions of the near-equatorial nightside are exposed to plasma. Plasma in the nightside and terminators is actually more energetic upon surface impact: a high reconnection rate at Mercury places the magnetic separatrix between the planetary field and IMF very near the planet's nightside, $\sim 1\text{-}3 R_M$ above the surface according to MESSENGER data (Slavin et al., 2010). Under this intense but steady-state driving, magnetospheric models suggest that large portions of the nightside are regularly bombarded by the energetic ions and electrons of the plasma sheet (Figure 10). Access to the nightside is accentuated under active magnetospheric conditions.

A simulation study of electron transport from the solar wind through Mercury's magnetosphere for solar wind conditions similar to the first two MESSENGER flybys of Mercury showed that precipitating electron fluxes were of the order $10^{10} \text{ cm}^{-2}\text{s}^{-1}$, with average energies 100's to $\sim 1000 \text{ eV}$, as illustrated in Figure 11 (Schrifer et al. 2010). Precipitating electron energies were generally lower during the first MESSENGER flyby when the IMF had a northward tilt, and were on average higher during the second flyby, when the IMF had a southward tilt (both cases had a large radial component to the IMF). These same results can be used to predict surface depletion of alkali species within Mercury's regolith.

The timescale for circulation of plasma, magnetic flux, and energy from the dayside magnetosphere to the magnetotail and, later, back to the dayside magnetosphere ("Dungey cycle"), is very short, $\sim 1 - 2$ minutes. These times are short compared to diffusive or gardening process rates therefore, even brief changes effected in the magnetosphere by reconnection have an opportunity to alter the surface over long timescales.

The Sun through time

Variations in the Sun's photon and solar wind output affects each process discussed above, including temperature, particle, and photon fluxes. The properties of the dynamic solar wind change on time scales ranging from hours to many millennia. Because wind evolution is directly tied to dynamic changes in the Sun, solar wind measurements can reveal internal solar processes. By examining solar variability using the sunspot record or proxies such as ice cores, solar wind traits can be inferred and correlated with planetary surface processing over

time. This section examines how the solar output has varied over these time scales and implications for the effectiveness of weathering processes on Mercury's surface.

Short time scale variations

Transient evolution: Short time variability, on the order of hours, originates from the scale-length of coronal structures and the plasma's evolution as it propagates through the inner heliosphere. Slower and faster streams may interact leading to compressive fluctuations or rarefaction regions. Coronal mass ejections (CMEs) are probably the dominant perturbations near Mercury. They can be hurled into space at 2000 km/s or more and their dynamic interactions can lead to large plasma pressures, which can overwhelm the magnetic protection of the planet, as modeled in Fig. 12.

Solar rotation time scale: Solar rotation should have important recurring heliospheric effects near the planet. Coronal holes have lifetimes of several solar cycles, so their associated fast solar wind streams are observed in subsequent solar rotations. CMEs have a tendency to erupt from certain solar longitude ranges; given the 33.9-day average synodic solar rotation period with respect to Mercury and accounting for Mercury's orbital eccentricity, solar plasma features should affect Mercury with this periodicity.

Solar cycle time scale: Solar wind properties, like composition, change during the solar cycle. For example, the helium abundance increases from <2% during solar minimum to ~4.5% at solar maximum (Aellig et al., 2001), and the in-ecliptic solar wind transitions from purely non-coronal hole wind at solar minimum to a mixture of the two types at maximum. The flux of anomalous and galactic cosmic rays detected at Earth depends on the solar cycle modulation, Φ , which quantifies the energy lost by particles entering the heliosphere (Gleeson and Axford, 1968). Φ is higher when the Sun is more active and the solar wind carries a stronger magnetic field through the inner heliosphere and the flux of low-energy GCRs (<10⁴ MeV/nucleon) reaching Earth decreases (Beer et al., 2006). More recently, the intensity of GCRs in the previous solar minimum exceeded that of the last five decades, indicating much lower solar activity (Mewaldt et al., 2010).

Moderate time scale variations

Centurial time scale: Sunspots have been counted regularly by astronomers since the early 1600's, creating a record of solar activity spanning 4 centuries. During times of increased sunspot numbers, solar activity is high; solar activity has increased, on average, over the last century. Periods of minimal solar activity occurred at the turn of the 18th, 19th,

and 20th centuries, seemingly cyclic with a 90-year period; a prolonged absence of sunspots 1645-1715 is called the Maunder Minimum (Pulkkinen et al., 2001). Beyond sunspot numbers, geomagnetic indices measured over the last century indicate trends of solar activity (cf. Lockwood et al., 1999). These indices are used to derive the mean solar wind speed, assuming speed is related to the expansion of open magnetic flux in the heliosphere (Wang and Sheeley, 1990); apparently the mean magnetic field strength and solar wind speed have increased during the first half of the 20th century (Rouillard et al., 2007).

Millennial time scale: Cosmogenic radionuclides produced by the interaction of GCRs with Earth's atmosphere, such as ^{10}Be in ice cores and ^{14}C in tree rings, give a proxy record of solar activity going back at least 10,000 years. Longer time scales have been analyzed from meteorites. The proxies show that Φ has varied by more than a factor of 3 and was lower than it is now ~85% of the time. Solar activity was low about 7,000 years before present (BP), rising to a peak about 2,000 years BP (Steinhilber et al., 2008). Space weathering by solar wind plasma is expected to increase when the solar activity is high, while cosmic ray generation increases when solar activity is low. Overall cosmic ray variability is not expected to vary by orders of magnitude.

Long time scale variations

Galactic Time Scales: Theoretical and observational modeling studies show that the properties of the heliosphere, and therefore the interplanetary environment, are affected by the galactic environment of the Sun (e.g. Zank and Frisch 1999, Frisch and Slavin 2006). While the Sun has resided in a very low density hot region (Local Bubble, LB) for over 3 Myr, LB properties have varied; the Sun has encountered local interstellar clouds (LIC) where densities, temperatures, and magnetic field properties have changed (Frisch and Slavin 2006). Interactions of the heliosphere with the interstellar medium (ISM) affect the solar wind and particle environment experienced by the planets. Simulations where ISM properties were held constant to current values except for the density of interstellar hydrogen (H^0) (Zank and Frisch, 1999) show that changing H^0 density from current values of $\sim 0.2 \text{ cm}^{-3}$ to 10 cm^{-3} reduced the size of the heliospheric cavity (distance from Sun to the upstream termination shock) from current values of $\sim 80 - 120 \text{ AU}$ to $\sim 10 - 14 \text{ AU}$. Zank and Frisch (1999) also demonstrated that the heliospheric configuration becomes highly dynamical and unstable, where the formation, disappearance, and re-formation of the termination shock cycles with a timescale of ~ 280 days. Under current ISM conditions interstellar hydrogen is entirely ionized a few AU from the Sun; however in this simulation the interstellar hydrogen density at Earth

is $\sim 2 \text{ cm}^{-3}$, thus exposing Earth to bombardment by H^0 . There is evidence for higher magnetic field strengths within denser LIC, which would further decrease the heliospheric radius by one half to one third, depending on the magnetic field configuration (Zank and Frisch 1999), increasing exposure of the inner planets to interstellar particles.

Zank and Frisch's (1999) simulation showed that pickup ions completely dominate the thermodynamic character of the outer heliospheric solar wind, creating solar wind temperatures in excess of 10^5 K . This in turn creates an inward pressure gradient, causing the solar wind to decelerate much more than through mass-loading scenarios; thus density as a function of heliocentric distance no longer obeys the usual r^{-2} dependence.

Interactions with LIC also increase the cosmic-ray flux at 1 AU (Zank and Frisch 1999), in two ways: (1) the increased pick-up ion population increases the ACR population, and (2) GCRs are no longer significantly modulated by an extended solar wind with reduction in the size of the heliospheric cavity (Zank and Frisch 1999). Evidence for past interactions of the solar system with LIC has been interpreted from Earth's geologic record. Spikes in ^{10}Be concentration in Antarctic ice core samples at 33,000 and 60,000 years ago have been attributed to an increase in cosmic-ray flux on Earth's atmosphere (Raisbeck et al. 1987, Sonett et al. 1987, Zank and Frisch 1999, Frisch and Slavin 2006). The increased cosmic-ray flux can be produced by changes in the Sun's galactic environment.

While studies of the effects of changes in the Sun's galactic environment have focused on the repercussions for Earth's climate, there will also be affects throughout the solar system. The effects at Mercury's orbit have not been quantified, but the timescales are on the order of millions to billions of years during the time of regolith formation for both Mercury and the Moon.

Geologic time scale: Lunar regolith samples record solar wind impacts that potentially date back nearly 4 Ga (Ga = billion years ago), and reveal the changing composition of the solar wind. The noble gases Xe and ^4He are enriched in samples of ancient regolith breccias by at least factors of 2, while the $^3\text{He}/^4\text{He}$ ratio is 20% lower than more recent (1.5-3.5 Gyr younger) soil samples (Kerridge et al., 1985). Assuming Xe and ^4He are accelerated by a stronger Coulomb drag than required by other noble gases (Geiss, 1973), the composition differences indicate that solar wind fluxes were higher in the past (Geiss, 1974).

Additional clues about the Sun over geologic time scales comes from studies of solar analog stars, mostly from the Sun in Time observation project (Ribas et al. 2005, Güdel 2007, Guinan and Engle 2009, Wood 2006, and references therein). The Sun entered the main sequence at 4.6 Ga. The bolometric luminosity at zero-age main-sequence (ZAMS) was $\sim 70\%$

of its present-day output (Siess et al. 2000, Ribas et al. 2005), meaning that the optical and infrared thermal outputs were 30% lower. However, the ZAMS Sun rotated faster than now, generating enhanced magnetic activity, which induces higher fluxes in the UV, EUV, and X-ray output of a star; such emissions may have been 10x, 100x, and 1000x higher than present levels, respectively (Ribas et al. 2005, Güdel 2007).

In addition, enhanced high-energy emissions and frequent flares typical of young stars also produce more powerful particle winds (Ribas et al. 2005). While stellar winds from solar analog stars have not been directly measured, indirect measurements through their interactions with the interstellar medium (Wood et al. 2001, 2002, Wood 2006, Ribas et al. 2005) indicate the coronal mass-loss rates for several solar analog stars. From these, Wood et al. (2002) propose that the mass-loss rate of the Sun has followed a power law proportional to t^{-2} , indicating that the solar wind may have been 1000 times more massive than now (Wood et al. 2002, Ribas et al. 2005). Young, solar analog stars exhibit explosive, episodic releases of plasma, generating non-thermal, high-energy particles, similar to current solar CMEs, but hundreds of times stronger and more frequent (Audard et al. 2000, Ribas et al. 2005).

Figs. 13 and 14 compare estimates of solar output over time with major geologic time periods and events from asteroids, and the Moon, which permits us to evaluate regolith exposure and alteration by solar processes described above (applicable to Mercury to the degree we can tie Mercury's geologic history to the lunar time scale). The Nectaris Basin formed on the Moon 4.1 – 3.9 Ga, and the Imbrium Basin ~3.85 Ga (Chapman et al. 2007, Stoffler and Ryder 2001). As many as ten basins may have formed between these two events. Orientale formed somewhat after Imbrium, but two thirds of the recognized lunar basins formed before Nectaris (Chapman et al. 2007). Thus the Late Heavy Bombardment (LHB) ended ~3.85 to 3.8 Ga; it commenced before Nectaris, but how long before is quite uncertain (4.1 Ga is adopted in Figs. 13 and 14). (An LHB-like period in the asteroid belt apparently began somewhat earlier than on the Moon and also lasted longer, ~4.2 to 3.5 Ga [Chapman et al. 2007]). The period of lunar volcanism has been partially constrained by dates of basalts from Apollo samples, which range from 3.8 to 3.15 Ga (Stoffler and Ryder 2001). As samples of surface or near-surface basalts, their dates represent the end of volcanism in their localities, so volcanism may have been active earlier.

There are no samples to constrain ages of geologic features on Mercury. Assuming that the timing of the lunar LHB, and that diagnostic size distributions for the bombarding populations on the Moon all apply to Mercury (Marchi et al., 2009), then the Mercury's

Caloris Basin formed late during the LHB, perhaps ~ 3.95 Ga, with the interior and surrounding volcanic plains emplaced ~ 3.8 Ga.

All these ancient geologic events occurred when the Sun's high-energy output was much greater than now and alteration of the surficial regolith by particle and photon bombardment processes must have been far greater. However, it is unclear to what degree such surficial regolith processes may be discerned from periods during and before the LHB, or even during later periods of extensive volcanism. It is also unclear what volumetric fraction of lunar and Mercurian materials may have been reworked (e.g. what fraction of upper crustal materials may have been depleted of alkalis or what fraction of FeO was converted to nanophase Fe) and to what depth. Since major cratering and volcanism ended on the Moon and Mercury, the surficial regolith has been gardened to depths of meters as described in an earlier section; only in isolated places was surficial regolith formation punctuated by a large (>10 km) crater. Prior to the end of volcanism, multiple lava flows meters thick, cumulatively up to kms thick, were emplaced, the vast bulk of which (depending on individual flow depths and time intervals between flows) were not processed by surface exposure and regolith gardening. Until late during the LHB, near-saturation of the lunar and Mercurian surfaces by giant impact basins and their extensive ejecta blankets and sculpturing formed megaregoliths km to tens of km thick. Assuming the size distribution of ancient meteoroids and micrometeoroids was similar to that today, the immediate surfaces of these volcanic and impact deposits were presumably churned to depths of cm to meters, but the bulk of the volcanic deposits and megaregolith was never located within mm of the surface and thus was not subject to solar processing. (The "shallow" size distribution for craters $>\sim 10$ km diameter does not churn the megaregolith the way smaller impacts garden the surficial regolith [Chapman et al. 2007].)

The comparisons in Figs. 13 and 14 show that the solar output was orders of magnitude higher during the heavy bombardment period when regolith formation, especially at meter to km scales, was being formed. During this period the optically active portion of the regolith (mm deep) was also being generated and overturned to substantial depths. Lunar regolith samples show evidence for this period of higher solar activity (Geiss 1974, Kerridge et al. 1985). Thus the surface of both objects have been subjected to solar-induced weathering processes during their regolith formation periods. We must await quantitative modeling of these regolith processes to estimate what fraction of upper crustal material has been processed. Perhaps rare regolith breccias from the Moon (and even Mercury, if relevant meteorites from Mercury are found) can provide insight to ancient events. In either case,

Mercury has been subjected to a qualitatively, on the order of magnitudes, more reducing environment than the Moon over their regolith formation histories.

Connections to the processes

The composition, energy, and flux of the different solar wind and photon components are summarized in Table 3 for the Moon, Mercury, and main belt asteroid region (2.7 AU central distance). The table correlates these components with the surface alteration processes. While the table shows that the particle energies are the same across this region of the solar system, impact energies are not equivalent. For example, protons are accelerated when they cross Mercury's cusp regions (Masetti et al. 2007). Lunar impact energies of ~ 1 keV have a corresponding energy of ~ 3 -7 keV on Mercury (Masetti et al. 2007). Mercury's proximity to the Sun exposes its surface to 5.2 to 11.9 times more solar flux at perihelion and aphelion, respectively, compared to the Moon. This translates to:

- § higher temperatures on Mercury (~ 100 to 700K, Morrison 1970; Davies et al. 1978) than the Moon (~ 100 to 400K, Keihm and Langseth 1973; Chase et al. 1974, 1976),
- § higher particle and photon fluxes than the Moon (by a $1/r^2$ factor).

The higher temperatures affect micrometeoroid impact and DIET processes. Cintala (1992) calculated the ratio of pure liquid produced during impact events at 100K vs 700K to be 1:1.3, implying a 30% greater production of melt products, such as agglutinates, on Mercury's day versus night side. A similar calculation for pure vapor production resulted in a ratio of 1:1.15, implying 15% more vapor products, such as grain patinas, on the day versus the night side. Differences in impact velocity between the Moon and Mercury contribute more to the variations in impact melt and vapor production, however temperature is also a non-negligible contributing factor. ESD experiments show linear increases in ion yields with increasing temperatures in the 350 – 550 K range (McLain et al. 2010; Yakshinskiy and Madey 2004, 2005).

Table 3. Solar Interactions at the Moon^a (1 AU), Mercury^b (0.4 AU), and the Main Belt (2.7 AU)

Solar Wind Component	Particle Composition	Energies (keV/nuc or keV)	Flux (cm ⁻² s ⁻¹) at 0.4 AU	Flux (cm ⁻² s ⁻¹) at 1AU	Flux (cm ⁻² s ⁻¹) at 2.7 AU	Ion Implantation	Sputtering	DIET
Coronal hole (fast) plasma	H ⁺ (96 - 98%) He ⁺ (2 - 4%) Heavy ions (<0.1%)	1.0-3.0	1.3×10^4	2×10^4	2.7×10^3	Reduces surface	Reduces surfaces ^a	Reduces surface
Non-coronal hole (slow) plasma	H ⁺ (96 - 99%) He ⁺ (1 - 4%) Heavy ions (<0.1%)	0.5-1.5	1.9×10^7	3×10^4	4.1×10^3		Removes alkalis	Removes alkalis
Transient plasma	H ⁺ (95%) He ⁺ (5%)	0.5-5.0	$6.3 \times 10^6 - 10^8$	$10^8 - 10^4$	1.4×10^7		Creates lattice defects	More efficient at higher temps.
Supra-thermal plasma (slow)	Solar wind comp.	3-50	$6.3 \times 10^7 - 10^8$	$10^7 - 10^5$	14 - 140	Creates lattice defects	Enhances diffusion	Enhanced by radiation damage to lattice
Supra-thermal plasma (fast)	Solar wind comp.	15-250	$6.3 \times 10^7 - 10^8$	$10^7 - 10^5$	140 - 14000		Production estimated to be ~ 0.01 molecule/ion at lunar fluxes ^d	Enhanced by higher energy and flux of radiation
High-energy particles	Varies	$10^2 - 10^3$	$6.3 \times 10^8 - 10^9$	$10^8 - 10^4$	$1.4 \times 10^7 - 10^6$	Enhances diffusion		
GCRs	H ⁺ (92%) He ⁺ (5%) Electrons (3%)	>10 ³	6.3×10^7	< $10^2 - 4$	1.4×10^7			
ACRs		$10^2 - 10^3$	variable	variable	variable			
UV-A	N/A	3.1 - 3.9	1.3×10^{12}	2×10^{11}	2.7×10^{11}	N/A	N/A	Only 10's of eV's needed
UV-B		3.9 - 4.4	1.5×10^{16}	2.5×10^{14}	3.4×10^{13}			
UV-C		4.4 - 12.4	6.3×10^{13}	10^{11}	1.4×10^{11}			
Soft X-rays		0.12 - 12	$6.3 \times 10^2 - 10^8$	$10^1 - 10^7$	140 - 14000			
Hard X-rays		12 - 120	60 - 6000	10 - 1000	1.4 - 140			

^aAssumes no residence time in the Earth's magnetosphere ^bAssumes no shielding from Mercury's magnetic field
A: Swords (2001), B: Johnson and Bargiola (1991)

Each of the processes listed in Table 3, along with micrometeoroid bombardment, work to reduce the regolith grains. The 5.2 to 11.9 higher solar radiation fluxes and the order of magnitude higher micrometeoroid flux all work to make Mercury's environment more highly reducing than that of the Moon or asteroids. Even over galactic and geologic time scales (time scales spanning the generation of the regolith) Mercury's environment has been more reducing than the lunar environment. The same holds for the removal of alkalis from the surface. In a "look down" approach, these processes will enrich the surface of Mercury in refractory species and low sputtering yield species such as Fe and Ti.

Mercury's Surface

We know about Mercury's surface properties from analyses and modeling of Earth-based reflectance and emission spectra, radar observations, and spacecraft imaging and spectral measurements. Modeling efforts constrain physical characteristics, such as porosity and grain size, and compositional properties, such as elemental abundances and mineral identifications. As discussed in previously, regolith porosity and grain size affect diffusion rates and trapping efficiencies, key moderators of weathering processes. Surface composition also affects weathering process rates, and in turn is altered by these same processes as evidenced by space weathering induced spectral changes. This section reviews constraints on the physical character and composition of Mercury's regolith and the observable effects of space weathering.

Regolith characteristics

Porosity, grain size distribution, surface roughness, and grain albedo and structure are constrained by analyzing and modeling photometric measurements. Reflectance measurements as a function of incidence, emission, and phase angles examined with Hapke's model (Hapke 1981, 1984, 1986, 2002) can provide measures of regolith grain characteristics that can be compared between solar system bodies. For example, comminution creates a grain-size characterization parameter, Y , given by

$$Y = \frac{\sqrt{3}}{\ln\left(\frac{r_l}{r_s}\right)}$$

(Bhattacharya et al. 1975), where r_l and r_s are the radii of the largest and smallest grains, respectively. The relationship between Y and the opposition width parameter, h , in the Hapke model is given by

$$h = -\left(\frac{3}{8}\right)Y \ln(\rho),$$

where ρ is the porosity of the optically-active top layer. The top of Figure 15 shows porosity estimates over a range of grain size ratios from the photometric analyses of Domingue et al. (2009) based on Mercury ground-based observations from Mallama et al. (2002), MESSENGER imaging data, and comparable lunar and S-type asteroid phase curves (Helfenstein and Veverka 1987, 1989, Hartman and Domingue 1998). Domingue et al. (2009) argue that the absolute value of the can not be derived from the model parameter; however, the results do indicate relative porosities between the planetary surfaces; showing Mercury's surface is less porous than either lunar or S-type asteroid surfaces, perhaps due to Mercury's higher surface gravity.

Application of Hapke's equations (Hapke modeling) provides a method to compare grain scattering properties with grain internal structures. The bottom of Figure 15 compares the single-particle scattering function parameters derived for Mercury, the Moon, and several asteroids with laboratory measures of these parameters linking them with particle scattering characteristics (McGuire and Hapke, 1995; Domingue et al., 2011). The grains of all three bodies show a moderate to high density of internal scatterers. (Internal scatterers are any boundary within the grain where the index of refraction changes, such as cracks, vesicles, mineral inclusions, or rims and patinas.) Mercury shows a distinct trend of increasing density of internal scattering centers with decreasing wavelength, constraining the sizes of these centers (Domingue et al. 2011). Domingue et al. (2011) postulate that if these centers are

created through weathering processes, then there is a lower density of structural boundaries in regolith grains on Mercury than on asteroids and a comparable density on Mercury and the Moon. These boundaries have a size distribution such that a significant portion is on scales of 400 nm or less (Domingue et al. 2011).

Grain sizes have also been estimated from comparing spectral data with laboratory measurements. Hapke modeling of visible to near-infrared ground-based observations of Mercury indicate that much of the regolith has grain sizes $\sim 20 \mu\text{m}$ (Warell et al. 2010), however comparing mid-infrared data with laboratory spectra indicate that regions on Mercury have grain sizes of 40 to 250 μm .

The Hapke surface roughness parameter (a measure of average surface tilt on size scales ranging from a few grain diameters to the resolution footprint of the observation detector) varies between 8° to 16° at 550 nm (Mallama et al. 2002, Warell 2004, Domingue et al. 2009, 2011). These values are smoother than the $20^\circ - 33^\circ$ derived for the Moon (Helfenstein and Veverka, 1987; Hartman and Domingue 1998) and asteroids (Helfenstein and Veverka 1989; Helfenstein et al. 1994, 1996; Domingue et al. 2002; Lederer et al. 2005). Domingue et al. (2011) interpreted these roughnesses to indicate surface texture differences between these planetary objects on the scale of regolith grains, postulating that finer grained dust on Mercury might clump together to produce conglomerate grains where the grain boundaries act as scattering centers thus increasing the scattering center densities. The clumping together of fine particles to form conglomerate grains would also decrease the average surface tilt at the several grain size scale, thus reducing the surface roughness value. Radar backscatter data are also influenced by surface roughness, in addition to topography and dielectric properties. Doppler spectrum and depolarized radar images confirm that Mercury has a regolith and indicates surface roughness value (average surface tilt on the scale of the radar wavelengths) of 4° in the smooth plains regions (Harmon 2007; Harmon et al., 2007) commensurate with the low values derived from photometry.

Regolith components

Mercury's cratered surface grossly resembles the Moon's (Murray et al. 1974) dominantly shaped by impacts. We can try to extrapolate to Mercury what we know about the lunar regolith. Lunar soils average 25 – 30% agglutinates, 3 – 5% impact glasses, and 1 – 4% material of meteoritic origin (Haskin and Warren 1991). Extrapolating to Mercury must take higher impact speeds and greater fluxes into account. As discussed earlier, orders more melt and vapor are produced by the impacts on Mercury compared with the Moon. Since mature

lunar soils contain up to 60% agglutinates (McKay et al. 1991) conceivably Mercury's regolith, at some locations, has been converted entirely to glass; Cintala (1992) considers that it may retain little crystalline material. The higher flux of exogenic material implies that the meteoritic component of Mercury's regolith is higher on Mercury (5 – 20%, Noble et al. 2007), compared with the Moon.

Various volcanic glass spherules are found in lunar soils (e.g., Delano 1986), and numerous lunar pyroclastic deposits (fragmented rock formed by explosive volcanism) have been mapped and analyzed with photogeological and other remote-sensing techniques (e.g., Gaddis et al. 2003). Deposits with anomalous color and morphology consistent with pyroclastic emplacement are on Mercury (Head et al., 2008; Murchie et al., 2008; Head et al., 2009; Kerber et al., 2009). Therefore, explosive volcanic products such as pyroclastic beads and disrupted rock fragments, are also likely to be in Mercury's regolith.

Mercury's surface has been greatly deformed by contractional tectonics (e.g., Watters et al. 2009; Watters et al. 2009), indicated by lobate scarps, high-relief ridges, and wrinkle ridges. Thus comminution unrelated to impact cratering, i.e., fault gouge and/or cataclasites (metamorphic rock comminuted by high mechanical stress) created through frictional action along fault planes may contribute slightly to Mercury's regolith. Mass wasting down slopes affects the lunar regolith, so probably also on Mercury, possibly enhanced by endogenic Mercury-quakes.

Composition

What little we know of Mercury's bulk crustal and surface composition is inferred from ground-based reflectance observations, color imaging observations from Mariner 10 and MESSENGER, and spectroscopic flyby data from MESSENGER's MASCS, NS, and GRS instruments. These provide a few constraints on elemental and mineral composition, but identification of specific minerals remains elusive, as we review below in the context of space weathering effects.

It has been inferred that Mercury's surface is low in iron based on microwave observations (Mitchell and dePater 1994), visible-near infrared reflectance spectra (McCord and Clark 1979, Vilas 1985, McClintock et al. 2008), and identification of minerals from thermal infrared Reststrahlen bands (Sprague et al. 2009). Such low amounts of surficial Fe contrast with Mercury's Fe-rich core, as inferred from its high density (Anderson et al., 1987). Mercury's surface albedo, for both mature and immature terrains, averages 10 – 15% darker than the lunar near-side (Warell et al. 2004, 2010, Denevi and Robinson 2008), which has a

bimodal albedo distribution (highlands versus maria) absent on Mercury. Denevi and Robinson (2008) found that young, Kuiperian age ray craters on Mercury are 30- 50% darker than analogous Copernican age ray craters on the Moon. These differences may mean (1) Mercury's regolith is of inherently darker material, (2) darkening processes have progressed farther on Mercury than the Moon, or (3) both.

We first consider iron (Fe) and titanium (Ti) abundances (from both elemental and mineral perspectives) and then discuss plausible regolith darkening agents and constraints on silicates, oxides, sulfides, and glasses.

Iron & Titanium

The abundances of Fe and Ti on Mercury's surface are key to deciphering Mercury's formation environment and the origin of its high bulk metal fraction. Fe and Ti can be present in different mineral forms ranging from silicates, to oxides, to metals. When Fe is bound to O in a silicate lattice (plagioclase and pyroxene), the resulting electronic transition produces a diagnostic spectral reflectance absorption band at $\sim 1 \mu\text{m}$. This feature is generally absent in whole disk spectra of Mercury (McCord and Clark 1979, Vilas 1985, McClintock et al. 2008, 2009), and in disk-resolved MASCs spectra (McClintock et al. 2008, 2009). Warell et al. (2006), however, did report a shallow absorption feature from 0.8 to 1.3 μm (centered at 1.1 μm) in two disk-resolved observations, suggesting that iron-bearing silicates may be localized (Warell et al. 2006, Boynton et al. 2007). Spectral deconvolution models of mid-infrared ground-based measurements show some solutions containing hedenbergite ($\text{FeCaSi}_2\text{O}_6$), a calcium-iron pyroxene, at the $\sim 30\%$ level. At this concentration, however, it should also produce a 1 μm feature in the near-infrared. Ground-based observations of Mercury are severely hampered by adverse conditions due to Mercury's proximity to the Sun. Observations are made either low to the horizon through a large airmass or during daytime. Detection of an absorption feature near 1 μm is hampered by a nearby terrestrial atmospheric water absorption.

Near-ultraviolet and visible MESSENGER spectra show a downturn from the visible into the near-ultraviolet that could be attributed to oxygen-metal charge transfer (OMCT, McClintock et al. 2008). This feature is exhibited only by transition metals (Burns 1993), the most abundant of which in the Earth-Moon system is iron. McClintock et al. (2008) suggest that the absorption edge seen in MESSENGER spectra is due to low-abundance Fe-bearing (FeO) silicates; limits based on reflectance spectra range from $\sim 3 \text{ wt}\%$ (Blewett et al. 1997),

to less than 2% (Warell and Blewett 2004, McClintock et al. 2008). Hapke modeling of first flyby MASCS spectra with laboratory mineral spectra yield between 1 – 8% FeO (Warell et al. 2010), depending on modeled mineral combinations.

Ti sometimes substitutes for Fe, though usually present as an oxide, TiO_2 . TiO_2 concentration has been inferred to be quite low from near-IR and microwave data (Warell and Blewett, 2004; Mitchell and de Pater, 1994). Blewett et al. (1997) modeled near-IR data yielding a TiO_2 abundance of ~1% or less, confirmed by Warell and Blewett (2004). In contrast, Chase et al. (1976) interpreting active and passive microwave data, concluded that Mercury's surface might have combined $\text{FeO}+\text{TiO}_2$ of ~20 wt.%, though Chase possibly overlooked other microwave absorbers which could be important (Elachi, 1987). In spectral deconvolution modeling of mid-infrared measurements, Sprague et al. (2009) find model solutions commensurate with a rutile (TiO_2) abundance of 37% in some areas. Warell et al.'s (2010) modeling of MASCS spectra with Hapke's equations found modeling solutions with 25% TiO_2 , much higher than the modeling estimates of Warell and Blewett (2004) based on near-infrared ground observations.

Beyond considerations of FeO and TiO_2 , there may be higher abundances of Fe and Ti in other forms. A reanalysis of Mariner 10 spectral data (Robinson and Lucey, 1997), calibrated relative to the Moon (Denevi and Robinson, 2007), strongly suggests that much of Mercury's surface has a spectrally neutral opaque phase consistent with, but not exclusive to, Fe-Ti oxides such as ilmenite (FeTiO_3) or ulvöspinel (Fe_2TiO_4) (Robinson et al. 2008 and Denevi et al. 2009). Using spectral mixing models, Denevi et al. (2009) show that Mercury's Intermediate Terrain (IT) may have up to 15 vol.% ilmenite-equivalent abundance and dark Low Reflectance Material (LRM) material perhaps up to 40 vol.%. Spectral deconvolution modeling of mid-infrared spectra of radar bright region "C" show good model matches with compositions including perovskite (CaTiO_3).

MESSENGER's Neutron Spectrometer (NS) has also been used to study Fe and Ti on Mercury's surface. It measures neutrons created by cosmic ray spallation reactions in the top meter of Mercury's surface. Thermal neutrons, the downscattered products of the initial fast neutrons, are highly sensitive to neutron absorbing elements, of which Fe and Ti are typically the most abundant in planetary materials. During the first flyby, NS measured thermal neutrons near (0°lon, 0°lat), finding a total neutron absorption of $45 - 81 \times 10^{-4} \text{ cm}^2/\text{g}$ (Lawrence et al., 2010). Converted to equivalent ilmenite content, this implies ~7 – 18 wt.% ilmenite, broadly consistent with Denevi et al. (2009). Alternatively, the neutron absorption could be 8 – 22 Fe-equivalent wt.% or 3 – 8 Ti-equivalent wt.% (most probable values being

14 and 5 Fe- or Ti-equivalent wt.%, respectively). These estimates, however, have not considered low or even trace quantities of other strongly neutron adsorbing elements that, in principle, could be responsible for the measured absorption.

Table 4. Estimates of surface iron and titanium content on Mercury.*

Reference	Measurement Type	FeO (wt %)	TiO ₂ (wt %)	FeO + TiO ₂ (wt %)
McCord and Adams (1972a,b); McCord and Clark (1979)	1 μ m absorption	≤ 6		
Chase et al (1976)	Microwave loss tangent			$\sim 20\%$
Hapke (1977)	1 μ m absorption	$\sim 3-6$		
Blewett et al. (1997)	1 μ m absorption	~ 3	$< \sim 1$	~ 4
Warell and Blewett (2004)	1 μ m absorption, Hapke modeling	< 2	< 1	
Warell et al. (2006)	1 μ m absorption	$> \sim 5$		
McClintock et al. (2008)	1 μ m absorption	$< 2-3$		
Sprague et al. (2009)	Mid-IR modeling	$\sim 2 - 5$	< 24	
Warell et al. (2010)	Hapke modeling	$1 - 8$	< 25	
		Fe (wt %)	Ti (wt %)	Fe + Ti (wt %)
Jeanloz et al. (1995)	Microwave loss tangent			< 6
Lawrence et al. (2010)	Neutron absorption	$8 - 22$	$3 - 8$	19
Rhodes et al. (2011)	Gamma-ray emission	$3 - 8$	$2 - 5$	

*Reflectance observations provide measurements of the equivalent oxide content of the silicate portion of the uppermost optical surface of the regolith, whereas microwave, neutron spectrometer, and gamma-ray spectrometer observations (Jeanloz et al., 1995; Lawrence et al., 2009; Rhodes et al., 2009) provide measurements of the bulk properties of the regolith (microwave observations penetrate 2 to 20 cm depth where as neutron and gamma-ray observations sample 10's of cm up to 1 m, depending on composition).

MESSENGER's Gamma-Ray spectrometer has probably (but not certainly) detected both Fe and Ti in Mercury's equatorial regions, 6 and 4 wt%, respectively, with one-sigma

error bars about half those values (Rhodes et al. 2010). Such Fe and Ti abundances limits are near the lower estimates from the NS modeling. While neither NS nor GRS can distinguish the mineral form of Fe or Ti, they do establish their probable elemental presence within Mercury's regolith. Table 4 summarizes all observations concerning Fe and Ti near Mercury's surface. The NS/GRS estimates contrast sharply with the mineralogical estimates based on infrared reflectance and emission spectral modeling, although the latter are from data highly affected by space weathering processes, not quantitatively considered in the modeling.

Metals (nanophase iron)

Mercury's regolith may well have Fe in the form of npFe^0 due to space weathering processes. Even if there is no native FeO within Mercury's regolith, meteorites could bring in, and account for 1-5% FeO in the regolith (Noble and Pieters 2003, Noble et al. 2003). Experiments by Noble et al. (2001) show that concentrations as low as 0.05 wt% npFe^0 are sufficient to influence reflectance properties.

Hapke (2001) estimated ~0.5 wt% of npFe^0 within Mercury's regolith, similar to the Moon, based on theoretical modeling and comparisons with ground-based spectra. Re-analysis by Warell (2003) found an upper bound to the npFe^0 abundance of <0.3 wt%, later revised to an estimate of 0.1 – 0.2 wt% (Warell and Blewett 2004, Warell et al. 2006). Analysis of MASCS spectra suggest a npFe^0 content on Mercury less than the Moon's (McClintock et al. 2008). Hapke modeling analyses by Warell and Blewett (2004) constrain the npFe^0 abundance to ~0.1 – 0.2 wt%, about half of the abundance in the average bulk lunar regolith (e.g. Morris 1980, Taylor et al. 2001a, Warell et al. 2010). Hapke modeling of MASCS first flyby spectra indicate an npFe^0 abundance of ~0.065 wt% with small variations between mature and immature regions (Warell et al. 2010). All these estimates for npFe^0 are in addition to (or separate from) estimates of FeO cited earlier, model-dependent, and based on spectra with minimal to no diagnostic absorption features; they attempt to match the albedo and spectral slope, but require assumptions on mineral constituents.

Coupling Mie theory with the Hapke (2001) radiative transfer equations, Lucey and Riner (2011) modeled spectral effects of npFe^0 particles of different sizes. They predict that npFe^0 particles <50 nm redden spectral slopes and particles >50 nm darken, but do not redden, consistent with results of Noble et al. (2007). Applying their model to near-infrared MASCS spectra of Mercury, Lucey and Riner (2011) suggests the presence of 3.5 wt.% of npFe^0 in Mercury's regolith with 3 wt.% greater than 50 nm.

Table 5. Spectral affects of intermediate size npFe⁰ (Nobel et al. 2007).

Size range (nm)	Average size (nm)	Concentration (wt%)	Spectral Effect
5 – 15	8	0.02	Curvature in visible, $\lambda > 700$ nm unaffected
		0.1	Curvature in visible, $\lambda > 700$ nm unaffected
		0.2	Curvature in visible, $\lambda > 700$ nm unaffected
		>1	Reddening across all wavelengths
10 – 25	15	0.02	Steep curvature develops in visible, $\lambda > 750$ nm unaffected
		0.1	Spectra redden curvature becomes less extreme and extends to longer wavelengths
		0.2	Spectra lose curvature and become increasingly linear
		>1	Spectra become increasingly dark with convex shape
25 – 50	35	<0.1	Slightly curved in visible and red-sloped in IR (similar to 10 – 25 particle size with 0.1 concentration)
		~0.1 – 1.0	Linear, highly red slope spectrum
		>1	Increasingly dark, convex shaped spectrum
20 – 200	40	0.02	Nearly linear with slightly red slope
		>0.02 - < 1.89	Progressively lower albedo, slight increase in red slope for $\lambda > 1000$ nm
		1.89	Convex continuum

Spectral effects of npFe⁰ concentration and particle size have been quantified by lab measurements (e.g. Noble et al. 2007). Small (< 10 nm diameter) npFe⁰ particles dramatically redden visible spectra but do not affect infrared spectra (Noble et al. 2007) while npFe⁰ particles >40 nm diameter lower albedo across the visible-infrared spectrum while not affecting the continuum's shape (i.e. no spectral reddening is detected). Spectral changes induced by intermediate-sized particles depend on concentration (Table 5). Studies of mixed sizes show behavior as expected for the average size, biased slightly towards large particle effects. These measurements were done on transparent, silicate gel spheres; spectral effects of

npFe⁰ in a more opaque mineral matrix, such as oxides, has not been quantified experimentally. In Lucey and Riner's (2011) model, varying opaque abundances shows that spectral darkening effects of >50 nm npFe⁰ dominate over the darkening effects of opaques; their model matches observations with opaque concentrations of 0 to 24 wt.%.

Noble et al. (2007) conclude that even at small concentrations the size of npFe⁰ particles influences reflectance properties. Lucey and Riner (2011) claim that all the darkening on Mercury could be entirely, but not necessarily, due to large grain npFe⁰. Lunar soil studies show npFe⁰ particles in agglutinates are at least twice as large as those in grain rims, ~7 nm and ~3 nm diameter, respectively (Keller and Clemett 2001, Noble et al. 2007). In some lunar agglutinates they may approach 100 nm diameter (Taylor et al. 2001a, 2001b, Noble et al. 2007); they may be large within agglutinates because grains with npFe⁰-bearing rims are melted to form the agglutinates and the npFe⁰ coalesces to form larger particles (Taylor et al. 2001a, 2001b, Noble et al. 2007).

For Mercury, where impacts produce significantly more melt and vapor than for the Moon, and where we expect more agglutinates and vapor-deposited rims, it is plausible that npFe⁰ will be larger grained (cf. the theoretical study of Lucey and Riner, 2011). Also there are such temperature effects as Ostwald ripening, through which npFe⁰ blebs coalesce and grow (Noble and Pieters 2003). Mercury's hot temperature could drive up npFe⁰ particle sizes, especially in the hottest areas (low latitudes and the "hot poles"), where spectral differences would be expected. Contrasting with finer npFe⁰ grain sizes at cooler high latitudes and associated reddened spectral continuum, larger average npFe⁰ particles near the equator might result in a flatter, darker spectrum. MESSENGER flyby multispectral images (Robinson et al. 2008, Blewett et al. 2009, Denevi et al. 2009) have not yet revealed systematic latitudinal color contrasts consistent with Ostwald ripening, but interpretation is complicated by color variations associated with compositional units and by high-reflectance crater rays. Starukhina and Shkuratov (2003) noted that continued growth of iron grains to sizes ~0.1 to 1.0 μm would cause a decrease in absorption and an increase in scattering. This effect might make "overmatured" soils brighter.

Noble et al. (2007) show that the combination of small npFe⁰ particles in rims with larger npFe⁰ particles in agglutinates accounts for the shape of lunar soil spectra. Considering telescopic spectra of Mercury, they predict Mercury's regolith to have more and larger npFe⁰ grains than the Moon, while S-class asteroid spectra should have slightly smaller npFe⁰ particles than the Moon, agreeing with the paucity of agglutinates in regolith breccia meteorites (e.g. Basu and McKay 1983) and evidence that solar wind irradiation is the

dominant weathering process on asteroids. Recent laboratory analyses of regolith breccia meteorites support these predictions. Noble et al. (2011) found small, though highly scarce, npFe^0 in mineral rims within these meteorites.

Silicates (plagioclase, pyroxenes, olivines)

Silicates, such as plagioclase (feldspar), pyroxene, and olivine, are indicated for Mercury's surface by emission and reflectance spectra (Sprague et al. 1994, 2002, 2007, 2009; Emery et al. 1998; Warell and Blewett 2004; Warell et al. 2006,). Feldspar emissions in the mid-IR were reported (Emery et al. 1998) and 14 – 28 wt% Na- and K-bearing feldspars were estimated for different locations based on spectral deconvolution model comparisons with laboratory spectra (Sprague et al. 2009). Ground-based mid-IR telescopic data have been interpreted to reveal magnesium-bearing orthopyroxenes, calcium-bearing clinopyroxenes, sodium-bearing plagioclase, and minor amounts of magnesium-rich olivine (Sprague et al. 2002, 2009). Olivine has been indicated by mid-IR emission features compared with laboratory spectra of Mg-rich olivines (Emery et al. 1998; Sprague et al. 2009). Slit observations at high north and south latitudes (Warell et al. 2006) indicate localized low-Fe, high-Ca pyroxenes. Exospheric identifications of Na, K (Potter and Morgan, 1985, 1986; Sprague et al. 1989) and Mg (McClintock et al., 2009) support the presence of minerals bearing these cations, although surface concentrations cannot be quantified based on exospheric measurements. Table 6 summarizes the current evidence for various silicate mineral assemblages.

Examples of the mid-infrared (top) and near-infrared (bottom) spectra, upon which these silicate mineral identifications are based, are displayed in Figure 16. These mineral identifications rely on comparisons with spectral measurements of minerals taken at room temperature, under standard photometric geometries (incidence, emission, and phase angle values of 0° , 30° , 30° , respectively), and have not been exposed to a weathering environment; conditions which do not match those of Mercury's surface or surface observations. The mineral quantities derived from the mid-infrared modeling should also produce detectable features in the near-infrared, which are not observed. While this discrepancy could be attributed to the differences between laboratory conditions and Mercury's surface, this has not been proven. Studies of the affects of temperature, photometry, and weathering at both mid- and near-infrared wavelengths is required to resolve this discrepancy.

Oxides and opaques

As noted above, Mercury's low albedo suggests its regolith may contain a spectrally neutral opaque component (Warell et al. 2006, Robinson et al. 2008, Denevi et al. 2009). Low iron- and titanium-bearing oxides (such as ilmenite (FeTiO_3), perovskite (CaTiO_3), ulvöspinel (Fe_2TiO_4), armalcolite ($(\text{Mg,Fe})\text{Ti}_2\text{O}_5$), and ferropseudobrookite (FeTiO_5)) have been offered as plausible candidates (McClintock et al. 2008, Robinson et al. 2008, Denevi et al. 2009, Sprague et al. 2009). Hapke modeling of MESSENGER MASCS data suggest the possible presence of lunar-like opaques at <10% level (Warell et al. 2010). Riner et al. (2009) argue that neither ilmenite, ulvöspinel, armalcolite, or ferropseudobrookite can be the sole darkening agents, since 20 – 50% abundances would be required to match measured reflectance properties. They derive an abundance of ilmenite needed to darken immature lunar highland sample material to match Mercury's reflectance at 490 nm of 27 – 38 wt% (18.5 – 21.9 equivalent wt% Fe + Ti), at the high-end or above the MESSENGER NS and GRS estimates. Alternate opaque minerals include geikielite (MgTiO_3), the magnesian end-member of a solid-solution series with ilmenite, and anosovite (Ti_3O_5), which forms a solid-solution series with armalcolite (Riner et al. 2009). Because laboratory reflectance data are lacking for these alternative, Mg-rich oxides, Riner et al. (2009) did not estimate abundances for these opaques on Mercury.

Lucey and Riner (2011) modeled spectra by varying amounts and sizes of npFe^0 and amounts of opaques and compared with MASCS near-IR spectra, showing that Mercury's albedo and spectral slope could be matched with 0 – 24 wt.% opaque. The best spectral matches were for 3 wt.% large npFe^0 and 0.5 wt% small npFe^0 , regardless of the opaque content in the model. They predict 4 – 6 wt.% opaque content if all npFe^0 is from these oxides rather than from silicates (Lucey and Riner, 2011).

Table 6. Silicate Estimates

Reference	Data source	Plagioclase	Pyroxene	Olivine
Sprague et al. 1994	Emission spectra	Na-bearing feldspar	enstatite	
Emery et al. (1998)	Emission spectra	Feldspar and feldspathoids		Mg-rich indicated
Warell et al. (2006)	Reflectance		Ca-rich	

	spectra		clinopyroxene	
Sprague et al. (2009)	Mid-IR modeling	K-spar within Caloris Basin, Na-bearing plagioclase various locations	Ca-rich clinopyroxene, Hedenbergite, Mg-rich orthopyroxene	
Warell et al. (2010)	Hapke modeling of reflectance spectra	35 – 70% Na-plag (orthoclase) Up to 70% pyroxene and ilmenite bearing glasses	≤ 30% Mg-rich clinopyroxene < 5 % Mg-rich orthopyroxene <21% MnO (hedenbergite)	minute amounts in the lab glasses used in the model

Warell et al.'s (2010) modeling suggests abundances for other oxides, such as SiO₂ (40-50 wt%), Al₂O₃ (10-35 wt%), and MnO (<21 wt%). GRS flyby data show silica (Si) at 23.8 wt% (Rhodes et al. 2011). Sprague et al. (2009) estimated SiO₂ content from mid-IR spectra as 49 wt% to 55 wt%, above that obtained from the visible-near-IR modeling, with both well above the GRS estimates. A possible explanation for the disagreements is that the mid-infrared data are whole-disk, whereas the GRS data are just for some equatorial regions.

Darkening agents

Here we consider additional darkening agents to help explain Mercury's low albedo. Beyond the low-iron oxides, impact glasses including agglutinates, and npFe⁰ discussed earlier, clinopyroxenes with strongly absorbing cations (such as Mn and Cr), temperature effects, and meteoritic material are also possibilities (Helbert and Maturilli 2009; Warell et al. 2010).

Riner et al. (2009) argue that Mercury's low albedo and apparent low Fe content argues against the formation of Fe, Ti-rich oxides, which would require the co-existing silicates to also be Fe rich (Riner et al. 2009), which is contra-indicated by the lack of a 1 μm band. Ilmenite displays a reflection peak near 1 μm. Hapke modeling by Riner et al. (2009)

shows that 16 – 40 wt% ilmenite is needed to completely mask the 1 μm feature in a lunar highland soil with 5.14 wt% FeO. More Mg-rich oxides with low-Fe silicates, possibly combined with some fine-grained ilmenite to mask the ferrous iron 1 μm absorption, is more geochemically plausible (Riner et al. 2009).

Spectral darkening effects within lunar soils have been attributed to the presence of glass, especially in the form of agglutinates, and npFe^0 . Hapke modeling of MASCS spectra suggests a $\sim 20 - 45\%$ abundance of low-Fe, low-Ti agglutinitic glass (Warell et al. 2010). Abundance estimates for npFe^0 based on spectral modeling, range from 0.065 wt% (Warell et al. 2010) to $\sim 0.1 - 0.2$ wt% (Warell and Blewett 2004) to 3.5 wt% (Lucey and Riner 2011). Noble et al. (2007) show that for npFe^0 amounts between 0.02% and 1.89%, npFe^0 grain sizes of ~ 40 nm, albedo is lowered and the spectral slope is only slightly reddened above 1000 nm.

Clinopyroxenes with strongly absorbing cations, such as Mn and Cr, are additional possible darkening agents (Warell et al. 2010). Since manganese is also a strong neutron absorber, it would affect NS estimates of Fe and Ti abundances deduced from the MESSENGER NS data but not from GRS data. Discrepancies between the GRS and NS estimates discussed earlier leave room for other neutron absorbers within Mercury's regolith (such as Sm, Gd, Zn, Mn, and Pb).

With Mercury's proximity to the Sun, temperature effects must also be considered, including Ostwald ripening of npFe^0 grains. Helbert and Maturilli (2009) examined mid-IR emission from labradorite (a possible Mercury analog) at temperatures, up to 420° C revealing emissivity changes with temperature. Their samples were visibly and significantly darker at Mercury's dayside temperatures. Near-infrared reflectance properties from 400 – 2500 nm have been measured in the laboratory for pyroxene and olivine over a temperature range of 80 – 448 K (Singer and Roush 1985). These measurements show that absorption features broaden with increasing temperature (Singer and Roush 1985). It is unknown if at Mercury's daytime surface temperatures if absorption features could broaden sufficiently to appear to lower the continuum albedo.

Estimates of meteoritic contributions to Mercury's regolith range between 5 to 20% (Noble et al. 2007). This contribution would include carbonaceous material from both asteroidal and cometary sources at a potentially significant percentage to contribute to the darkening of Mercury's regolith. This darkening agent would be ubiquitous to all geologic units.

Discussion

Mercury's crustal composition is key to understanding the processes involved in Mercury's planetary formation. Remote sensing of the regolith, derived from crustal bedrock, is the sole means for inferring Mercury's crustal composition. But the regolith's physical, chemical, and mineralogical nature has been space weathered, processed, and altered, thus obscuring direct evidence of crustal composition. To interpret these space weathering on Mercury's regolith, an understanding of Mercury as an interactive system is needed. This paper has reviewed this system, tying together the exospheric formation processes, the space environment, and surface composition. The same processes that form and sustain the exosphere weather Mercury's surface. The space environment, including the solar wind and Mercury's intrinsic magnetic field, moderates these processes.

The expected physical, chemical, and mineralogical regolith traits resulting from weathering processes are summarized in Table 7. On the physical side, the higher micrometeoritic flux and impact velocities on Mercury compared with the Moon should produce more impact melt products, such as agglutinates, glasses, and vapor coatings (rims or patinas) on regolith grains. Impacts should create and garden Mercury's regolith perhaps an order-of-magnitude more efficiently than the lunar regolith, readily providing new crustal material for exospheric species production and burying matured and reduced material. Both solar wind irradiation and deposition of impact vapors and melts on surficial grains create patinas that affect reflectance spectra. Mercury's magnetic field does not completely shield the surface from ion radiation. Nightside equatorial regions are exposed to ion precipitation from the tail region, even under nominal conditions (See Figure 11). Dayside high latitudes are exposed to the solar wind under nominal conditions, increasingly so when the Sun is active. Under active solar periods these dayside high latitude cusp regions can extend equator ward, exposing mid latitude regions to the solar wind. The proton flux at Mercury can be an order of magnitude higher than at the Moon (see Table 3), when solar wind has access to the surface. Thus qualitatively, we expect grain surfaces at Mercury to be more highly radiation damaged, resulting in thicker patinas.

Other physical alterations to Mercury's regolith include greater grinding into finer size fractions ($< 45 \mu\text{m}$) than observed in lunar soils by the higher micrometeorite flux and velocities. Smaller grains have higher volume diffusion rates, thus more quickly reducing the regolith in volatiles, including alkalis.

Table 7. Summary of Mercury surface alterations

Alteration Type	Process	Effect
Physical/Structural	Micrometeoritic bombardment	Greater abundance of agglutinates and impact melt products compared with lunar soil
	Micrometeoritic bombardment	Larger portion of regolith in “finest fraction” (<20 μ m) compared with lunar soil
	Solar wind irradiation, Micrometeoritic bombardment	Thicker amorphous, reduced rims or patinas on grains compared with lunar soil
	Solar wind irradiation	Increased lattice defects within regolith grains compared with lunar grains
Chemical	Ion implantation	H implantation, at saturation level?
	Physical/chemical sputtering	Removal of H, OH,
	DIET, physical/chemical sputtering	Depletion of alkalis
	DIET	Repository for exospheric species
Mineralogical	Micrometeoritic bombardment, ion implantation, chemical sputtering	Reduction products, such as npFe ⁰

Chemical alteration depends on both diffusion rates and lattice structural defects. The more efficient melting (compared with the Moon) produces higher amorphous content, hence higher diffusion rates. The greater radiation flux increases lattice structural defects, enhancing DIET and diffusion rates, and creating sites for adsorption of exospheric species. MESSENGER orbital observations will improve our knowledge of balances between removal-vs.-deposition of regolith material, deposition of material into the exosphere, and removal from the exosphere to both the surface and solar wind.

Space weathering changes mineralogy, for instance reducing minerals and depleting alkalis (efficiency depends on relative rates of removal and implantation, as discussed above). The presence of npFe^0 , a reduction process product, will depend on the initial FeO content within the regolith. This reduction product is also the major contributor to spectra modifications. Assessing Fe content (in silicate, oxide, and metal forms) depends on different measurement techniques, including vis-IR measurements in which diagnostic absorption bands are diminished with increasing space weathering maturity. Neutron absorptions and gamma-ray emission features constrain Fe contents but not mineralogy, which is especially important for understanding Mercury's formational history.

Many condensation and accretion models fail to predict Mercury's high density and large core (Lewis 1988). Possible explanations include: (1) fractionation by mechanical sorting of silicate and metal grains by aerodynamic drag in the solar nebula at the onset of planetesimal accretion (Weidenschilling 1978), (2) preferential vaporization of silicates in the outer crust (after planetary differentiation) by a hot solar nebula with removal of the silicate fraction by the solar wind (Cameron 1985, Fegley and Cameron 1987), and (3) removal of the outer silicate crust after planetary differentiation by a giant impact (Wetherill 1988, Benz et al. 1988). The fractionation hypothesis does not selectively fractionate between major silicate minerals (Lewis 1988). For instance, Lewis (1988) says the silicate portion would include 3.6 – 4.5% alumina, ~1% alkali oxides, and 0.5 – 6% FeO. The vaporization hypothesis would strongly enrich the crust in refractory elements and severely deplete it in alkalis and FeO (Fegley and Cameron 1987, Lewis 1988). The giant impact hypothesis might yield a residual crust of mantle composition with little enhancement of refractories (Lewis 1988) but with a severe depletion of the Ca, Al, and volatile alkalis that would have been in the pre-impact crust. FeO contents, however, would coincide with the primordial oxidation state of the material present at the time and location of Mercury's accretion (Lewis 1988), which might be the same as for the fractionation hypothesis, perhaps 0.5 – 6%. Table 8 summarizes the compositional variations predicted for each formation model.

As have been shown, space weathering will alter such initial compositions at Mercury's surface, for example, by converting FeO to npFe^0 , thus biasing determination of crustal FeO. Also, alkalis may be preferentially removed compared with refractories. Thus to distinguish between these formation models we must understand the influence of each weathering process over the formation history of the regolith and the links between the exosphere and surface.

Table 8. Element abundance versus formation model predictions

Element	Fractionation Model	Vaporization Model	Impact Model
FeO	0.5 – 6% (as predicted by condensation models)	Severely depleted	0.5 – 6% (equivalent to the primordial oxidation state at accretion)
Refractory elements (Ca, Al, & Ti)	3.6 – 4.5% Al	Strongly enriched	No enhancement, Severe depletion of Ca & Al
Alkalis (Na & K)	~1% (alkalis oxides)	Severely depleted	Severely depleted in volatile alkalis metals

References

- M. M. Abbas, D. Tankosic, P. D. Craven, A. C. LeClair, J. F. Spann, *Astrophys. J.* 718, 795 (2010)
- M. R. Aellig, A. J. Lazarus, J. T. Steinberg, *Geophys. Res. Lett.*, 28, 2767 (2001)
- I. I. Alexeev, E. S. Belenkaya, J. A. Slavin, H. Korth, B. J. Anderson, D. N. Baker, S. A. Boardsen, C. L. Johnson, M. E. Purucker, M. Sarantos, S. C. Solomon, *Icarus* 209, 32 (2010)
- E. Anders, *Icarus* 24, 363 – 371 (1975)
- B. J. Anderson, M. H. Acuna, H. Korth, M. E. Purucker, C. L. Johnson, J. A. Slavin, S. C. Solomon, R. L. McNutt Jr., *Science*, 321, 82 (2008)
- B. J. Anderson, M. H. Acuna, H. Korth, J. A. Slavin, H. Uno, C. L. Johnson, M. E. Purucker, S. C. Solomon, J. M. Raines, T. H. Zurbuchen, G. Gloeckler, R. L. McNutt Jr., *Space Sci. Rev.* 152, 307 (2009)
- J. D. Anderson, G. Columbo P. B. Esposito P. B. Lau, G. B. Trager, *Icarus* 71, 337 (1987)
- Apollo Soil Survey, *Earth Planet. Sci. Lett.* 12, 49 (1971)
- M. Audard, M. Gudel, J. J. Drake, V. L. Kashyap, *Astrophys. J.*, 541, 396 (2000)

- D. N. Baker, D. Odstreil, B. J. Anderson, C. N. Arge, M. Benna, G. Gloeckler, J. M. Raines, D. Schriver, J. A. Slavin, S. C. Solomon, R. M. Killen, and T. H. Zurbuchen, *J. Geophys. Res.* 114, A10101 (2009)
- S. J. Bame, J. R. Asbridge, W. C. Feldman, J. T. Gosling, *J. Geophys. Res.*, 82, 1487 (1977)
- A. Basu, *J. Sed. Petrol.* 46, 694 (1976)
- A. Basu, D. J. DesMarais, J. M. Hayes, W. G. Meinschein, *The Moon* 14, 129 (1975)
- A. Basu, D. S. McKay. *Meteoritics* 18, 263 (1983)
- D. Bäuerle, *Laser processing and Chemistry*, (Springer, New York, 2000) 1 – 788
- J. Beer, M. Vonmoos, R. Muscheler, *Space Science Reviews*, 125, 67 (2006)
- R. Behrisch, K. Wittmaack, in *Sputtering by Particle Bombardment III*, ed. By R. Behrisch and K. Wittmaack (Springer-Verlag, New York, 1991), pp. 1-13
- R. G. Behrisch, B. M. Maderlechner, U. Scherzer, M. T. Robinson, *Appl. Phys.* 18, 391 (1979)
- W. Benz, W. L. Slattery, A. G. W. Cameron, *Icarus* 74, 516 (1988)
- R. P. Binzel, S. J. Bus, T. H. Burbine, J. M. Sunshine, *Science* 273, 946 – 948 (1996)
- R. P. Binzel, A. Morbidelli, S. Herouane, F. E. DeMeo, M. Birlan, P. Vernazza, C. A. Thomas, A. S. Rivken, S. J. Bus, A. T. Tokunaga, *Nature* 463, 331 – 334 (2010).
- C. Björkas, K. Vörtler, D. Nishijima, R. Doerner, *New J. of Physics* 11, 123017 (2009)
- D. T. Blewett, B. W. Denevi, M. S. Robinson, C. M. Ernst, M. E. Purucker, S. C. Solomon, *Icarus*, 209, 239 (2010)
- D. T. Blewett, B. Ray Hawke, P. G. Lucey, P. G., *Meteoritics & Planet. Sci.* 37, 1245 (2002)
- D. T. Blewett, P. G. Lucey, B. Ray Hawke, G. G. Ling, M. S. Robinson, *Icarus* 129, 217 (1997)
- D. T. Blewett, M. S. Robinson, B. W. Denevi, J. J. Gillis-Davis, J. W. Head, S. C. Solomon, G. M. Holsclaw, W. E. McClintock, *Earth & Planet. Sci. Lett.* 285, 272 (2009)
- P. Bochsler, *Space Sci. Rev.* 85, 291 (1998)
- P. Borin, G. Cremonese, F. Marzari, M. Bruno, S. Marchi, *Astron. Astrophys.* 503, 259 (2009)
- W. V. Boynton, A. L. Sprague, S.C. Solomon, R. D. Starr, L. G. Evans, W. C. Feldman, J. I. Trombka, E. A. Rhodes, *Space Sci. Rev.* 131, 85 (2007)
- R. Brunetto, F. Romano, A. Blanco, S. Fonti, M. Martino, V. Orofino, C. Verrienti, *Icarus* 180, 546 (2006)
- M. H. Burger, R. M. Killen, R. J. Vervack, E. T. Bradley, W. E. McClintock, M. Sarantos, M. Benna, N. Mouawad, *Icarus* 209, 63 (2010)

- B. J. Butler, *J. Geophys. Res.* 102, 19283 (1997)
- A. G. W. Cameron, *Icarus* 64, 285 (1985)
- H. Campins, M. S. Kelley, Y. Fernandez, J. Licandro, K. Hargrove, *Earth Moon and Planets* 105, 159 – 165 (2009)
- W. D. Carrier III, G. R. Olhoeft, W. Mendell, In *Lunar Sourcebook*, ed. By G. H. Heiken, D. T. Vaniman, B. M. French (Cambridge Press, New York, 1991) p.736
- C. R. Chapman, *MAPS* 31, 699 – 725 (1996)
- C. R. Chapman, *Ann. Rev. Earth & Planet. Sci.* 32, 539 (2004)
- C. R. Chapman, J. W. Salisbury, *Icarus* 19, 507 – 522 (1973)
- C. R. Chapman, B. A. Cohen, D. H. Grinspoon, *Icarus* 189, 233 (2007)
- S. C. Chase, E. D. Miner, D. Morrison, G. Munch, G. Neugebauer, M. Schroeder, *Science* 185, 142 (1974)
- S. C. Chase, S. C., E. D. Miner, D. Morrison, G. Munch, and G. Neugebauer, *Icarus*, 28, 565 (1976)
- H. Chen, A. Aleksandrov, Y. Chen, S. Zha, M. Liu, T. M. Orlando, *J. Phys. Chem. B*, 109(22), 11257 (2005)
- A. F. Cheng, O. Barnouin-Jha, N. Hirata, H. Miyamoto, R. Nakamura, H. Yano, *Geophys. Res. Lett.* (2007) doi:10.1029/2007GL029559
- D. B. Chrisey, G.K. Hubler, *Pulsed laser deposition of thin films* (Wiley, New York, 1994)
- M. J. Cintala, *J. Geophys. Res.* 97, 947 (1992)
- R. N. Clark, *Science* 326, 562 (2009)
- P. J. Coleman, Jr., G. Schubert, G.T. Russell, L.R. *Moon*, 4, 419 (1972)
- J. E. Colwell, S. Batiste, M. Horanyi, S. Robertson, S., Sture, *Rev. Geophys.* 45, 26 (2007)
- D. H. Crider, R. R. Vondrak, *J. Geophys. Res.* 108, 5070 (2003)
- D. R. Criswell, *Proc. Lunar Sci. Conf.* 3rd, 2671 (1972)
- D. R. Criswell, in *Photon and Particle Interactions with Surfaces in Space*, ed. By R. J. L. Grard (D. Reidel Publishing Co., Dordrecht, 1973) pp. 545–556
- A. Czechowski, I. Mann, *Astrophys. J.* 714, 89 (2010)
- M. E. Davies, D. E. Dwornik, D. E. Gault, R. G. Strom, *Atlas of Mercury*. (U. S. Government Printing Office, Washington D. C., 1978)
- J. Delano, *J. Geophys. Res.* 91, D201 (1986)
- B. W. Denevi, M. S. Robinson, *Icarus* 197, 239 (2008)

- B. W. Denevi, M. S. Robinson, S. C. Solomon, S. L. Murchie, D. T. Blewett, D. L. Domingue, T. J. McCoy, C. M. Ernst, J. W. Head, T. R. Watters, N. L. Chabot, *Science* 324, 613 (2009)
- M. I. Desai, G. M. Mason, J. E. Mazur, J. R. Dwyer, *Astrophys. J. Lett.*, 645, L81 (2006)
- D. J. DesMarais, J. M. Hayes, W. G. Meinschein, *Proc. Lunar Sci. Conf.* 5th, 1811 (1974)
- J. M. Devine, D. S. McKay, J. J. Papike, *J. Geophys. Res.* 87, A260 (1982)
- D. L. Domingue, P. L. Koehn, R. M. Killen, A. L. Sprague, M. Sarantos, A. Cheng, E. T. Bradley, W. E. McClintock, *Space Science Reviews* 131, 161 (2007)
- W. W. Duley, D. A. Williams, *Mon. Not. R. Astron. Soc.* 260, 37 (1993)
- P. Evenson, M. Garcia-Munoz, P. Meyer, K. R. Pyle, J. A. Simpson, *Astrophys. J. Lett.*, 275, L15- (1983)
- J. P. Emery, A. L. Sprague, F. C. Witteborn, J. E. Colwell, R. W. H. Kozlowski, D. H. Wooden, *Icarus* 136, 104 (1998)
- S. Epstein, H. P. Taylor, Jr., *Proc. Lunar Sci. Conf.* 3rd, 1429 (1972)
- S. Epstein, H. P. Taylor, Jr., *Proc. Lunar Sci. Conf.* 6th, 1771 (1975)
- W. M. Farrell, T. J. Stubbs, R. R. Vondrak, G. T. Delory, J. S. Halekas, *Geophys. Res. Lett.* 34, L14201 (2007)
- B. Fegley, A. G. W. Cameron, *Earth & Planet. Sci. Lett.* 82, 207 (1987)
- U. Feldman, E. Landi, N. A. Schwadron, *J. Geophys. Res.-Space*, 110 (A9), 7109 (2005)
- L. A. Fisk, G. Gloeckler, *Astrophys. J. Lett.*, 640, L79- (2006)
- L. A. Fisk, G. Gloeckler, *Astrophys. J.* 686, 1466 (2008)
- L. A. Fisk, G. Gloeckler, N. A. Schwadron, *Astrophys. J.* 720, 533 (2010)
- P. C. Frisch, J. D. Slavin, *Astrophys. Space Sci. Trans.* 2, 53 (2006)
- L. R. Gaddis, M. I. Staid, J. A. Tyburezym, B. Ray Hawke, N. E. Petro, *Icarus* 161, 262 (2003)
- I. Garrick-Bethell, J. W. Head, C. M. Pieters, *Eos Trans. AGU* 90 (52), Fall Mtg. Suppl., abstract GP34A-04 (2009a)
- I. Garrick-Bethell, J. W. Head, C. M. Pieters, *Lunar Planet. Sci.* 41, abstract 2675 (2010)
- D. E. Gault, J. E. Guest, J. B. Murray, D. Dzurisin, M. Malin, *J. Geophys. Res.* 80, 2444 (1975)
- J. Geiss, *Proc. 13th Int. Cosmic Ray Conf.*, 5, 3375 (1973)
- J. Geiss, *LPI Contributions* 195, 110 (1974)
- J. Geiss, G. Gloeckler, R. von Steiger, *Space Sci. Rev.* 72, 49 (1995)
- G. R. Gladstone, G.R, LAMP Team, *Science* 330, 472 (2010)

- L. J. Gleeson, W. I. Axford, *Astrophys. J.* 154, 1011 (1968)
- G. Gloeckler, J. Geiss, E. C. Roelof, L. A. Fisk, F. M. Ipavich, K. W. Ogilvie, L. J. Lanzerotti, R. von Steiger, B. Wilken, *J. Geophys. Res.* 99, 17637 (1994)
- G. Gloeckler, J. Geiss, *Space Sci. Rev.* 97, 169 (2001)
- G. Gloeckler, T. H. Zurbuchen, J. Geiss, *J. Geophys. Res.-Space*, 108, 1158 (2003)
- K. A. Goettel, in *Mercury*, ed F. Vilas, C. R. Chapman, M. S. Matthews (University of Arizona Press, Tucson, 1988), p. 794
- N. Grevesse, A. J. Sauval, *Adv. Space Res.*, 30, 3 (2002)
- D. Gruen, B. Siskind, R. Wright, *J. Chem. Phys.* 65, 363 (1976)
- M. Gudel, *The Living Reviews in Solar Physics* 4, arXiv:0712.1763v1 (2007)
- E. F. Guinan, S. G. Engle, *Proceedings IAU Symposium No. 258*, (2009)
- J. S. Halekas, D. L. Mitchell, R. P. Lin, et al. *Geophys. Res. Lett.* 29 (10), 1435 (2002)
- B. Hapke, *Phys. Earth, Planet. Inter.* 15, 264 (1977)
- B. Hapke, *J. Geophys. Res.* 106, 10039 (2001)
- J. K. Harmon, P. J. Perillat, M. A. Slade, *Icarus* 149, 1 (2001)
- J. K. Harmon, M. A. Slade, *Science* 258, 640 (1992)
- J. W. Head, S. L. Murchie, L. M. Prockter, M. S. Robinson, S. C. Solomon, R. G. Strom, C. R. Chapman, T. R. Watters, W. E. McClintock, D. T. Blewett, J. J. Gillis-Davis, *Science* 321, 69 (2008)
- J. W. Head, S. L. Murchie, L. M. Prockter, S. C. Solomon, C. R. Chapman, R. G. Strom, T. R. Watters, D. T. Blewett, J. J. Gillis-Davis, C. I. Fassett, J. L. Dickson, G. A. Morgan, L. Kerber, *Earth & Planet. Sci. Lett.* 285, 227 (2009)
- G. H. Heiken, *Rev. Geophys. Space Phys.* 13, 567 (1975)
- G. H. Heiken, D. T. Vaniman, B. M. French, B.M., *Lunar Sourcebook*, (Cambridge Univ. Press, New York, 1991) p. 736
- J. Helbert, A. Maturilli, *Earth Planet. Sci. Lett.* 285, 347 (2009)
- T. Hirori, S. Sasaki, *Meteorit. Planet. Sci.*, 36, 1587 (2001)
- L. Holmlid, *Planet. Space Sci.* 54, 101 (2006)
- L. Hood, G. Schubert, *Science*, 208, 49 (1980)
- L. Hood, C. Williams, *Proc. Lunar Planet. Sci. Conf. 19th*, 99 (1989)
- L. L. Hood, C. T. Russell, P. J. Coleman Jr., *J. Geophys. Res.*, 86, 1055 (1981)
- F. Horz, M. Cintala, *Meteoritics* 32, 179 (1997)
- F. Horz, M. Cintala, T. H. See, F. Cardenas, T. D. Thompson, *J. Geophys. Res.*, 89, C183 (1984)

- R. M. Housley, E. H. Cirlin, R. W. Grant, Proc. Lunar Sci. Conf. 4th, 2729 (1973a)
- R. M. Housley, R. W. Grant, N. E. Patton, Proc. Lunar Sci. Conf. 4th, 2737 (1973b)
- R. L. Huguenin, *Proceedings of the Colloquium on Water in Planetary Regoliths*, Publ. 1976A77-17062, 33 (1976).
- F. M. Ipavich, et al., J. Geophys. Res., 103, 17205 (1998)
- R. Jeanloz, D. L. Mitchell, A. L. Sprague, I. dePater, Science 268, 1455 (1995)
- R. E. Johnson, R. Baragiola, Geophys. Res. Lett. 18, 2169 (1991)
- J. R. Jokipii, M. A. Lee Astrophys. J., 713, 475 (2010)
- S. Jovanovic, G. W. Reed, Jr., *Earth Planet. Sci. Lett.*, 16, 257 (1972)
- S. Jovanovic, G. W. Reed, Jr., *Proc. Lunar Planet. Sci. Conf* 10th, 636 (1979)
- S. Jovanovic, G. W. Reed, Jr., *Proc. Lunar Planet. Sci. Conf.* 10th, 1425 (1979)
- K. Kabin, T. I. Gombosi, D. L. DeZeeuw, K. G. Powell, Icarus, 143, 397 (2000)
- M. L. Kaiser, K. Goetz, C. Steyr, S. Bale, M. Maksimovic, AGU Fall meeting, abstract #SH52B-01. (2007)
- E. Kallio, P. Janhunen, 34th COSPAR Sci. Assembly, Second World Space Congress (abstract). (2002)
- S. J. Keihm, M. G. Langseth, Proc. Lunar Sci. Conf. 4th, 2503 (1973)
- K. Keil, H. Haack, E. R. D. Scott, Planet. Space Sci. 42, 1109 (1994)
- L. P. Keller, S. P. Clemett, Lunar Planet Sci. Conf., [CD-ROM], XXXII, abstract 2097 (1993)
- L. P. Keller, D. S. McKay, Science 261, 1305 (2001)
- L. Kerber, J. W. Head, S. C. Solomon, S. L. Murchie, D. T. Blewett, L. Wilson, Earth & Planet. Sci. Lett. 285, 263 (2009)
- J. F. Kerridge, R. H. Becker, R. O. Pepin, Meteoritics, 20, 682 (1985)
- R. M. Killen, T. H. Morgan, *Icarus*, 101, 293 (1993a)
- R. Killen, G. Cremonese, H. Lammer, S. Orsini, A. E. Potter, A. L. Sprague, P. Wurz, M. L. Khodachenko, H. I. M. Lichtenegger, A. Milillo, A. Mura, Space Sci. Rev. 132, 433 (2007)
- R. M. Killen, W. –H. Ip, Rev. Geophys. 37 (3), 361 (1999)
- R. M. Killen, M. Sarantos, A. E. Potter, P. Reiff, Icarus 171, 1 (2004)
- B. Klecker, E. Möbius, M. A. Popecki, *Space Sci. Rev.*, 124, 289 (2006)
- A. Kotarba, I. Kruk, Z. Sojka, J. Catalysis 221, 650-652.
- U. Krähenbühl, A. Grütter, H. R. von Gunten, G. Meyer, F. Wegmüller, A. Wytenback, Proc. Lunar Sci. Conf 8th, 3901 (1977)

- H. Lammer, P. Wurz, M. R. Patel, R. Killen, C. Kolb, S. Massetti, S. Orsini, A. Milillo, *Icarus* 166, 238 (2003)
- J. C. Laul, J. J. Papike, S. B. Simon, *Proc. Lunar Sci. Conf.* 12B, 389 (1981)
- D. J. Lawrence, W. C. Feldman, J. O. Goldsten, T. J. McCoy, D. T. Blewett, W. V. Boynton, L. G. Evans, L. R. Nittler, E. A. Rhodes, S. C. Solomon, *Icarus*, 209, 195 (2010)
- D. J. Lawrence, W. C. Feldman, J. O. Goldsten, S. C. Solomon, *Lunar Planet. Sci.* 40, 1761 (abstract). (2009)
- F. Leblanc, R. E. Johnson, *Icarus* 164, 261 (2003)
- P. Lee, *Icarus*, 124, 181 (1996)
- M. Le Feuvre, M. A. Wieczorek, *Icarus* 197, 291 (2008)
- C. Leinert, I. Richter, E. Pitz, B. Planck, *Astron. Astrophys.* 103, 177 (1981)
- S. T. Lepri, T. H. Zurbuchen, L. A. Fisk, I. G. Richardson, H. V. Cane, G. Gloeckler, *J. Geophys. Res.*, 106, 29231 (2001)
- M. Lockwood, R. Stamper, M. N. Wild, A. Balogh, G. Jones, *Astronomy and Geophysics* 40, 10- (1999)
- S. G. Love, D. E. Brownlee, *Science* 262, 550 (1993)
- A. Luhn, B. Klecker, D. Hovestadt, M. Scholer, G. Gloeckler, F. M. Ipavich, C. Y. Fan, L. A. Fisk, *Advances in Space Research*, 4, 161 (1984)
- T. E. Madey, B. V. Yakshinskiy, V. N. Ageev, R. E. Johnson, *J. Geophys. Res.* 103, 5873 (1998)
- R. H. Manka, in *Photon and Particle Interactions with Surfaces in Space* (D. Reidel Publishing Co., Dordrecht, 1973) pp. 347–361
- I. Mann, H. Kimura, D. A. Biesecker, B. T. Tsurutani, E. Grun, R. B. McKibben, J. –C. Liou, R. M. MacQueen, T. Mukai, M. Guhathakurta, P. Lamy, *Space Sci. Rev.* 110, 269 (2004)
- S. Marchi, R. Bruneto, S. Magrin, M. Lazzarin, D. Gandolfi, *Astron. Astrophys.* 443, 769 (2005)
- S. Marchi, A. Morbidelli, G. Cremonese, *Astron. Astrophys.* 431, 1123 (2005)
- E. Marsch, K.-H. Mühlhäuser, R. Schwenn, H. Rosenbauer, K.-H. Muehlhaeuser, W. Pilipp, F. M. Neubauer, *J. Geophys. Res.*, 87, 52 (1982)
- S. Massetti, S. Orsini, A. Milillo, A. Mura, *Planet. Space Sci.* 55, 1557 (2007)
- W. E. McClintock N. R. Izenberg, G. M. Holsclaw, D. T. Blewett, D. L. Domingue, J. W. Head, J. Helbert, T. J. McCoy, S. L. Murchie, M. S. Robinson, S. C. Solomon, A. L. Sprague, F. Vilas, *Science* 321, 62 (2008)

- W. E. McClintock, R. J. Vervack, Jr., E. T. Bradley, R. M. Killen, N. Mouawad, A. L. Sprague, M. H. Burger, S. C. Solomon, N. R. Izenberg, *Science*, 324, 610 (2009)
- D. J. McComas, B. L. Barraclough, H. O. Funsten, J. T. Gosling, E. Santiago-Muñoz, R. M. Skoug, B. E. Goldstein, M. Neugebauer, P. Riley, A. Balogh, *J. Geophys. Res.*, 105, 10419 (2000)
- D. J. McComas, H. A. Elliott, J. T. Gosling, D. B. Reisenfeld, R. M. Skoug, B. E. Goldstein, M. Neugebauer, A. Balogh, *Geophys. Res. Lett.*, 29, 1290, (2002)
- J. E. McCoy, D. R. Criswell, *Proc. Lunar Sci. Conf. 5th*, 2991 (1974)
- T. B. McCord, J. B. Adams, *Science* 178, 745 (1972a)
- T. B. McCord, J. B. Adams, *Icarus* 17, 585 (1972b)
- T. B. McCord, R. N. Clark, *J. Geophys. Res.* 84, 7664 (1979)
- D. S. McKay, G. Heiken, A. Basu, G. Blandford, S. Simon, R. Reedy, B. French, J. Papike, J. in *Lunar Sourcebook*, ed. G. H. Heiken, D. T. Vaniman, B. M. French (Cambridge University Press, New York, 1991).
- D. S. McKay, G. H. Heiken, R. M. Taylor, U. S. Clanton, D. A. Morrison, G. H. Ladle, *Proc. Lunar Sci. Conf. 3rd*, 983 (1972)
- J. L. McLain, A. L. Sprague, G. A. Grieves, D. Schriver, P. Travinicek, T. Orlando, J. *Geophys. Res.*, submitted. (2011)
- R. A. Mewaldt, *Adv. Space Res.*, 14, (10)737 (1994)
- R. A. Mewaldt, C. M. S. Cohen, G. M. Mason, A. C. Cummings, M. I. Desai, R. A. Leske, J. Raines, E. C. Stone, M. E. Wiedenbeck, T. T. von Rosenvinge, T. H. Zurbuchen, *Space Sci. Rev.*, 130, 207 (2007)
- R. A. Mewaldt, A. J. Davis, K. A. Lave, R. A. Leske, E. C. Stone, M. E. Wiedenbeck, W. R. Binns, E. R. Christian, A. C. Cummings, G. A. de Nolfo, M. H. Israel, A. W. Labrador, T. T. von Rosenvinge, *Astrophys. J. Lett.*, 723, L1 (2010)
- D. Mitchell, D., I. de Pater, *Icarus*, 110, 2 (1994)
- T. H. Morgan, H. Zook, A.E. Potter, *Icarus* 75, 156 (1988)
- L. V. Moroz, A.V. Fisenko, L.F. Semjonova, C.M. Pieters, N.N. Korotaeva, *Icarus*, 122, 366 (1996)
- R. V. Morris, *Proc. Lunar Sci. Conf. 7th*, 315 (1976)
- R. V. Morris, *Proc. Lunar Planet. Sci. Conf. 11th*, 1697 (1980)
- R. V. Morris, R. Score, C. Dardano, G. Heiken, *Handbook of Lunar Soils*. (JSC Publ. No. 19069, Planetary Materials Branch Publ. 67. NASA Johnson Space Center, Houston, 1983)

- D. Morrison, *Space Sci. Rev.*, 11, 271 (1970)
- N. Mouawad, M. H. Burger, R. M. Killen, A. E. Potter, W. E. McClintock, R. J. Vervack, Jr., E. T. Bradley, M. Benna, S. Naldu, *Icarus* 211, 21 (2011)
- S. L. Murchie, T. R. Watters, M. S. Robinson, J. W. Head, R. G. Strom, C. R. Chapman, S. C. Solomon, W. E. McClintock, L. M. Prockter, D. L. Domingue, D. T. Blewett, *Science* 321, 73 (2008)
- B. C. Murray, M. J. Belton, G. E. Danielson, M. E. Davies, D. E. Gault, B. Hapke, B. O'Leary, R. G. Strom, V. Suomi, N. Trask, *Science* 185, 169 (1974)
- S. K. Noble, C. M. Pieters, *Astron. Vestnik* 37, 34 English transl. in *Solar Sys. Res.* 37 (1), 31 (2003)
- S. K. Noble, C. M. Pieters, L. P. Keller, *Icarus* 192, 629 (2007)
- S. K. Noble, C. M. Pieters, L. A. Taylor, R. V. Morris, A. C. Carlton, D. S. McKay, L. P. Keller, *Meteoritics & Planet. Sci.* 36, 31 (2001)
- S. K. Noble, L. P. Keller, C. M. Pieters, *Meteoritics & Planet. Sci.* 37, Supplement, A110. (2002)
- J. J. Papike, S. B. Simon, C. White, J. C. Laul, *Proc. Lunar Sci. Conf.* 12, 409 (1981)
- J. J. Papike, S. B. Simon, J. C. Laul, *Rev. Geophys. Space Phys.* 20, 761 (1982)
- J. Papike, L. Taylor, S. Simon, in *Lunar Minerals in Lunar Sourcebook* ed. By G.H. Heiken, D. T. Vaniman, B. M. French (Cambridge Univ. Press, New York, 1991) p. 736
- C. M. Pieters, *J. Geophys. Res.*, 88, 9534 (1983)
- C. M. Pieters, J. N. Goswami, R. N. Clark, M. Annadurai, J. Boardman, B. Buratti, J.-P. Combe, M. D. Dyar, R. Green, J. W. Head, C. Hibbits, M. Hicks, P. Isaacson, R. Kilma, G. Kramer, S. Kumar, e. Livo, S. Lundeen, E., Malaret, T. McCord, J. Mustard, J. Nettles, N. Petro, C. Runyon, M. Staid, J. Sunshine, L. A. Taylor, S. Tompkins, P. Varanasi, *Science* 326, 568 (2009)
- C. M. Pieters, L. A. Taylor, *Geophys. Res. Lett.*, 30(20), 2048 (2003)
- C. M. Pieters, E. M. Fischer, O. Rode, A. Basu, *J. Geophys. Res.*, 98, 20,817 (1993)
- C. M. Pieters, L. A. Taylor, S. K. Noble, L. P. Keller, B. Hapke, R. V. Morris, C. C. Allen, D. S. McKay, S. Wentworth, *Meteorit. Planet. Sci.* 35, 1101 (2000)
- A. E. Potter, *Geophys. Res. Lett.* 22, 3289 (1995)
- A. Potter, T. H. Morgan, *Science* 229, 651 (1985)
- A. Potter, T. H. Morgan, *Icarus* 67, 336 (1986)
- T. I. Pulkkinen, H. Nevanlinna, P. J. Pulkkinen, M. Lockwood, *Space Sci. Rev.*, 95, 625 (2001)

- G. M. Raisbeck, F. Yiou, D. Bourles, C. Lorius, J. Jouzel, N. I. Barkov, *Nature* 326, 273 (1987)
- D. V. Reames, C. K. Ng, A. J. Tylka, *Geophys. Res. Lett.* 26, Issue 23, 3585 (1999)
- G. W. Reed, Jr., *Meteorit. Planet. Sci.* 34, 809 (1999)
- J. J. Rennilson, D. R. Criswell, *The Moon* 10, 121 (1974)
- I. Ribas, E. F. Guinan, M. Güdel, M. Audard, *Astrophys. J.* 622, 680 (2005)
- M. A. Riner, P. G. Lucey, S. J. Desch, F. M. McCubbin, *Geophys. Res. Lett.* 36, L02201, (2009)
- E. A. Rhodes, L. G. Evans, R. D. Starr, W. V. Boynton, D. K. Hamara, In: Programme with Abstracts, The Surface Composition of Mercury from Ultraviolet-Visible-Infrared Spectroscopy: State of the Art and Future Strategies, Università degli Studi di Parma, Parma Italy, pp. 32-33 (2009)
- E. A. Rhodes, L. G. Evans, L. R. Nittler, R. D. Starr, A. L. Sprague, D. J. Lawrence, T. J. McCoy, K. R. Stockstill-Cahill, J. O. Goldsten, P. N. Peplowski, W. V. Boynton, S. C. Solomon, Submitted to Planetary Space Science special issue. (2011)
- M. S. Robinson, P. G. Lucey, *Science* 275, 197 (1997)
- M. S. Robinson, S. L. Murchie, D. T. Blewett, D. L. Domingue, S. E. Hawkins, III, J. W. Head, G. M. Holsclaw, W. E. McClintock, T. J. McCoy, R. L. McNutt, Jr., L. M. Prockter, S. C. Solomon, T. R. Watters, *Science*, 321, 66-69, (2008)
- A. P. Rouillard, M. Lockwood, I. Finch, *J. Geophys. Res.*, 112, A05103, (2007)
- C. T. Russell, P.J. Coleman Jr., B.K. Fleming, L. Hilburn, G. Ioannidis, B.R. Lichtenstein, G. Schubert, *Proc. Lunar Sci. Conf. 6th*, 2955 (1975)
- M. Sarantos, R. M. Killen, D. Kim, *Space Sci.*, 55, 1584 (2007)
- M. Sarantos, R. M. Killen, W. E. McClintock, E. T. Bradley, R. J. Vervack, Jr., M. Benna, J. A. Slavin, *Planet. Spa. Sci.*, submitted. (2010)
- S. Sasaki, E. Kurahashi, *Adv. Space Res.* 33, Issue 12, 2152 (2004)
- S. Sasaki, K. Nakamura, Y. Hamabe, E. Kurahashi, T. Hiroi, *Nature*, 410 (6828), 555. (2001)
- S. Sasaki, T. Hiroi, K. Nakamura, Y. Hamabe, E. Kurahashi, M. Yamada, *Adv. Space Res.* 29, 783 (2002)
- S. Sasaki, E. Kurahashi, C. Yamanaka, K. Nakamura, *Adv. Space Res.*, 31 (12), 2537 (2003)
- R. Schwenn, in *Space and Solar Physics, Vol. 20, Physics of the Inner Heliosphere I*, ed. By R. Schenn, E. Marsch (Springer-Verlag Berlin Heidelberg, 1990)
- Y. Shao, J. Paul, *Appl. Surf. Sci.*, 72, 113 (1993)

- A. A. Sickafoose, J. E. Colwell, M. Hora'nyi, S. Robertson, *J. Geophys. Res.* 107(A11), 1408 (2002)
- L. Siess, E. Dufour, M. Forestini, *Astron. Astrophys.*, 358, 593 (2000)
- B. Siskind, D. Gruen, R. Varma, *J. Vac. Sci. Tech.* 14, 537 (1977)
- M. A. Slade, B. J. Butler, D. O. Muhleman, *Science* 258, 635 (1992)
- J. A. Slavin, R. E. Holzer, *J. Geophys. Res.* 84, 2076 (1979)
- J. A. Slavin, M. H. Acuna, B. J. Anderson, D. N. Baker, M. Benna, G. Gloeckler, R. E. Gold, G. C. Ho, R. M. Killen, H. Korth, S. M. Krimigis, R. L. McNutt Jr., L. R. Nittler, J. M. Raines, D. Schriver, S. C. Solomon, R. D. Starr, P. Travnicek, T. H. Zurbuchen, *Science*, 321, (2008)
- J. A. Slavin, M. H. Acuna, B. J. Anderson, D. N. Baker, M. Benna S. A. Boardsen, S.A., G. Gloeckler, R. E. Gold, G. C. Ho, H. Korth, S. M. Krimigis, R. L. McNutt Jr., J. M. Raines, M. Sarantos D. Schriver, S. C. Solomon, P. Travnicek, T. H. Zurbuchen, *Science*, 324, 606 (2009)
- J. A. Slavin, R. P. Lepping, C. -C. Wu, B. J. Anderson, D. N. Baker, M. Benna, S. A. Boardsen, R. M. Killen, H. Korth, S. M. Krimigis, W. E. McClintock, R. L. McNutt Jr., M. Sarantos, D. Schriver, S. C. Solomon, P. Travnicek, T. H. Zurbuchen, *Geophys. Res. Lett.*, 37, L02105, (2010a)
- J. A. Slavin, B. J. Anderson, D. N. Baker, M. Benna, S. A. Boardsen, G. Gloeckler, R. E. Gold, G. C. Ho, H. Korth, S. M. Krimigis, R. L. McNutt Jr., L. R. Nittler, J. M. Raines, M. Sarantos, D. Schriver, S. C. Solomon, R. D. Starr, P. Travnicek, T. H. Zurbuchen, *Science* 329, 665 (2010b)
- C. P. Sonett, G. E. Morfill, R. J. Jokipii, *Nature* 330, 458 (1987)
- A. L. Sprague, K. L. Donaldson Hanna, R. W. H. Kozlowski, J. Helbert, A. Maturilli, J. B. Warell, J. L. Hora, *Planet. Space Sci.* 57, 364 (2009)
- A. L. Sprague, J. P. Emery, K. L. Donaldson, R. W. Russell, D. K. Lynch, A.L. Mazuk, *Meteorit. Planet. Sci.* 37, 1255 (2002)
- A. Sprague, J. Warell, G. Cremonese, Y. Langevin, J. Helbert, P. Wurz, I. Veselovsky, S. Orsini, A. Milillo, *Space Sci. Rev.* 132, 399 (2007)
- A. L. Sprague, D. M. Hunten, K. Lodders, *Icarus* 118, 211 (1995)
- L. Starukhina, *J. Geophys. Res.* 106, 14701 (2001)
- F. Steinhilber, J. A. Abreu, J. Beer, *Astrophys. Space Sci. Trans.*, 4, 1 (2008)
- D. Stoffer, G. Ryder, *Space Sci. Rev.* 96, 9 (2001)

- D. Stöffler, A. Dischoff, V. Buchwald, A. E. Rugin, in *Meteorites and the Early Solar System*, ed By J. F. Kerridge, M. S. Matthews (University of Arizona Press, Tucson, 1988) pp. 165-202.
- D. Stöffler, K. Keil, E. R. D. Scott, *Geochim. Cosmochim. Acta* 55, 3845 (1991)
- G. Strazulla, E. Dotto, R. Binzel, R. Burnetto, M. A. Barucci, A. Blanco, V. Orofino, *Icarus* 174, 31 (2005)
- T. J. Stubbs, R. R. Vondrak, W. M. Farell, *Adv. Space Sci.* 37, 59 (2006)
- J. M. Sunshine, T. L. Farnham, L. M. Feaga, O. Groussin, F. Merlin, R. E. Miliken, M. F. A'Hearn, *Science* 326, 565 (2009)
- G. J. Taylor, E. R. D. Scott, In: *Treatise on Geochemistry, Volume 1: Meteorites, Comets, and Planets*, ed. By A. M. Davis (Elsevier, Amsterdam, The Netherlands, 2003) pp. 477–485
- L. A. Taylor, R. V. Morris, L. P. Keller, C. M. Pieters, A. Patchen, D. –H. Taylor, S. J. Wentworth, D. S. McKay, *Lunar Planet. Sci.* 31, abstract 1842. (2000)
- L. A. Taylor, C. M. Pieters, L. P. Keller, R. V. Morris, D. S. McKay, A. Patchen, S. J. Wentworth, *Meteorit. Planet. Sci.*, 36, 288 – 299. (2001a)
- L. A. Taylor, C. M. Pieters, L. P. Keller, R. V. Morris, D. S. McKay, *Geophys. Res. Lett.*, 106, 27985 (2001b)
- L. A. Taylor, C. M. Pieters, A. Patchen, D-H. S. Taylor, R. V. Morris, L. P. Keller, D. S. McKay, *J. Geophys. Res.* (2010) doi:10.1029/2009JE003427
- D. Vaniman, J. Dietrich, G. J. Taylor, G. Heiken, G. in *Lunar Sourcebook*, ed. By G. H. Heiken, D. T. Vaniman, B. M. French (Cambridge University Press, New York, 1991) p. 736
- P. Vernazza, R. P. Binzel, A. Rossi, M. Fulchignoni, M. Birlan, *Nature* 458, 993 (2009)
- F. Vilas, *Icarus* 64, 133- (1985)
- F. Vilas, in *Mercury*, ed. By F. Vilas, C. Chapman, M. Matthews (University of Arizona Press, Tucson, 1988) p. 794
- F. Vilas, E. A. Jensen, D. L. Domingue, L. A. McFadden, C. Runyon, W. W. Mendell, *Earth, Planets, Space* 60, 67 (2008)
- R. von Steiger, J. Geiss, *Advances in Space Research*, 13, 63 (1993)
- R. von Steiger, N. A. Schwadron, L. A. Fisk, J. Geiss, G. Gloeckler, S. Hefti, B. Wilken, R. F. Wimmer-Schweingruber, T. H. Zurbuchen, *J. Geophys. Res.*, 105, 27217 (2000)
- R. von Steiger, T. H. Zurbuchen, D. J. McComas, *Geophys. Res. Lett.*, 37, L22101 doi:10.1029/2010GL045389. (2010)
- Y.-M. Wang, N. R. Sheeley, *Astrophys. J.*, 355, 726 (1990)

- J. Warell, *Icarus* 161, 199 (2003)
- J. Warell, D. T. Blewett, *Icarus* 168, 257 (2004)
- J. Warell, A. L. Sprague, J. P. Emery, R. W. H. Kozlowski, A. Long, *Icarus* 180, 281 (2006)
- J. Warell, A. Sprague, R. Kozlowski, D. A. Rothery N. Lewis, J. Helbert, E. Cloutis, *Icarus* 209, 138 (2010)
- T. R. Watters, S. C. Solomon, M. S. Robinson, J. W. Head, S. L. Andre, S. A. Hauck, S. L. Murchie, *Earth & Planet. Sci. Lett.* 285, 283 (2009a)
- T. R. Watters, J. W. Head, S. C. Solomon, M. S. Robinson, C. R. Chapman, B. W. Denevi, C. I. Fassett, S. L. Murchie, R. G. Strom, *Science* 325, 618 (2009b)
- S. J. Weidenschilling, *Icarus* 35, 99 (1978)
- G. W. Wetherill, in *Mercury*, ed. By F. Vilas, C. R. Chapman, M. S. Matthes (University of Arizona Press, Tucson, 1988) p. 794
- D. H. White, *The Solar Output and Its Variation*. (Colorado Associated University Press, Boulder, 1977)
- B. E. Wood, *Space Science Rev.* 126, 3 (2006)
- B. E. Wood, J. L. Linsky, H. –R. Müller, G. P. Zank, *ApJ*, 547, L49 (2001)
- B. E. Wood, H. –R. Müller, G. Zank, J. L. Linsky, *ApJ*, 574, 412 (2002)
- P. Wurz, H. Lammer, *Icarus*, 164, 1 (2003)
- P. Wurz, J. A. Whitby, U. Rohner, J. A. Martín-Fernández, H. Lammer, C. Kolb, *Planet. Space Sci.* 58, 1599 (2010)
- P. Wurz, U. Rohner, J. A. Whitby, C. Kolb, H. Lammer, P. Dobnikar, J. A. Martín-Fernández, *Icarus* 191, 486 (2007)
- B V. Yakshinskiy, T. E. Madey, *Nature* 400, 642 (1999)
- B V. Yakshinskiy, T. E. Madey, *Surface Science* 451, 160 (2000)
- B V. Yakshinskiy, T. E. Madey, *Surface Science* 528, 54 (2003)
- B V. Yakshinskiy, T. E. Madey, *Icarus* 168, 53 (2004)
- B V. Yakshinskiy, T. E. Madey, *Surface Science* 593, 202 (2005)
- M. Yamada, S. Sasaki, H. Nagahara, A. Fujiwara, S. Hasegawa, H. Yano, T. Hiroi, H. Ohashi, H. Otake, *Earth Planets Space*, 51, 1255 (1999)
- G. P. Zank, P. C. Frisch, *Astrophys. J.* 518, 965 (1999)
- E. Zellner, L. Ronca, P. Levy, *J. Geophys. Res.* 71, 4855 (1996)
- L. Zhao, T. H. Zurbuchen, L. A. Fisk, *Geophys. Res. Lett.*, 36, L14104, (2009)
- H. A. Zook, *Proc. Lunar Sci. Conf.*, 6th, 1653- (1975)
- H. A. Zook, J. E. McCoy, *Geophys. Res. Lett.* 18 (11), 2117 (1991)

- T. H. Zurbuchen, L. A. Fisk, G. Gloeckler, R. von Steiger, *Geophys. Res. Lett.*, 29, 1352 (2002)
- T. H. Zurbuchen, P. Koehn, L. A. Fisk, T. Gombosi, G. Gloeckler, K. Kabin, *Adv. Space Res.* 33, Issue 11, 1884 (2004)